# From the lithosphere to the lower mantle: An aqueous-rich metal-bearing growth environment to form type IIb blue diamonds

Lucille Daver, Hélène Bureau, Églantine Boulard, Éloïse Gaillou, Pierre Cartigny, Daniele Pinti, Oulfa Belhadj, Nicolas Guignot, Eddy Foy, Imène Estève, et al.

# From the lithosphere to the lower mantle: an aqueous-rich metal-bearing growth environment to form type IIb blue diamonds

Lucille Daver[1,2*], Hélène Bureau[1], Églantine Boulard[1], Éloïse Gaillou[3], Pierre Cartigny[4], Daniele L. Pinti[2], Oulfa Belhadj[5], Nicolas Guignot[6], Eddy Foy[7], Imène Estève[1] and Benoit Baptiste[1]

[1] Institut de Minéralogie, de Physique des Matériaux et de Cosmochimie (IMPMC), Sorbonne Université, CNRS UMR 7590, 75252 Paris Cedex 05, France

[2] GEOTOP and Département des sciences de la Terre et de l'atmosphère, Université du Québec à Montréal, Montreal, QC, H3C 3P8, Canada

[3] MINES ParisTech, PSL Research University, Musée de Minéralogie, 75006 Paris, France

[4] Institut de Physique du Globe de Paris, Université de Paris, 75005 Paris, France

[5] Centre de recherche sur la conservation, Muséum National d'Histoire Naturelle, 75005 Paris, France

[6] Synchrotron Soleil, 91191 Gif-sur-Yvette, France

[7] Université Paris-Saclay, CEA, CNRS, NIMBE/LAPA, 91191, Gif-sur-Yvette, France

Corresponding author: Lucilledaver@hotmail.fr

Type IIb diamonds; blue diamonds; boron; nitrogen; mineral inclusions; aqueous fluids; Fe-Ni alloys; lithosphere.

**Abstract**. A study of five diamonds containing mineral and fluid inclusions, selected among forty-nine specimens from the Cullinan Mine, South Africa, was carried out to better document the origin and formation of type IIb diamonds. The combination of several in-situ non-destructive techniques was used to identify the mineralogy and the chemical composition of primary and secondary inclusions. These inclusions include breyite, larnite, graphite, Fe-Ni-Cu native metallic alloys, sulfides of the pyrrhotite group, Ni-rich oxide and potential hydrous ferric sulfates. A common and abundant hydrous fluid containing $H_2O + CH_4$ was also identified. From the various observations, we suggest that these type IIb diamonds grew in an aqueous oxidized fluid reacting with a reduced mantle characterized by low oxygen fugacity. Remnant pressures recorded in primary breyite by Raman shifts and XRD measurements enabled the calculation of minimal entrapment pressures of inclusions using elastic geothermobarometry. Applying pressure corrections caused by elastic relaxation, minimum trapping pressures from 4.9 GPa to 5.6 GPa were calculated, suggesting lithospheric depths consistent with the occurrence of numerous graphite inclusions. The association of breyite and larnite, which is often considered as an indicator of sublithospheric origin, also occurs at pressures of 6 GPa or lower in a carbonate/Ca-rich environment. The B-poor and N-absent features of type IIb diamonds do not support the classic subduction-related model of their formation. Whereas high-pressure minerals would host boron in cold subducting slabs, slabs are also important carriers of nitrogen into the deep mantle, with this latter element mostly absent in these diamonds. In our alternative model, the mantle is equally proposed to be the source of boron, while maintaining that metallic alloys or N speciation between fluid and melt would still prevent the incorporation of nitrogen, leading to the expression of the blue, boron-related and N-poor features of type IIb diamonds. The observed mineralogical assemblage neither proves sublithospheric origin nor excludes lithospheric depths of formation for these diamonds. Hence,

we propose that type IIb diamonds form in a mantle continuum, from sublithospheric to lithospheric depths.

## 1. Introduction

The study of natural diamonds and their mineral/fluid inclusions provides unique constraints on the mineralogy of the Earth's mantle from 120 km to approximately 800 km depth, i.e., from the lithosphere down to the lower mantle (Harte, 2010; Shirey et al., 2019). Diamonds are also a unique sample from which to infer the nature of parent metasomatic C-O-H-N-S fluids or melts percolating through the mantle (e.g., Schrauder and Navon, 1994; Cartigny et al., 2014; Smit et al., 2016; Stachel et al., 2017).

In addition to the traditional classification based on their nitrogen and boron content, diamonds are also classified based on the mineralogy and geochemistry of their solid and fluid inclusions. Most diamonds are of lithospheric origin (above 300 km depth) and are believed to grow in C-O-H-N-S fluids (see reference above). Lithospheric diamonds usually contain olivine, pyroxene, garnet, spinel and sulfides (e.g., Meyer, 1987; Stachel and Harris 2009) as typical mineral inclusions. Superdeep diamonds (formed at depths between 410 to 800 km) are rare and contain typically majorite garnet, ferropericlase, Ca-perovskite and bridgmanite (e.g., Shirey et al., 2013). The nature and composition of the parent fluids of sublithospheric diamonds are more difficult to assess because the oxygen fugacity should be much lower at these depths (approximately FMQ-5; Frost and McCammon, 2008). It is suggested that C, H and O in metal-saturated regions of the deep mantle are buffered to reduced compositions, with C being either dissolved into metallic liquids or existing as $CH_4$-rich fluids (e.g., Shirey et al., 2019).

Based on the traditional classification, blue diamonds are defined as type IIb, having almost no nitrogen, while the blue color results from the presence of boron ($\leq$ 8 ppm; Gaillou et al., 2012). Boron, which substitutes for carbon in the crystal lattice of diamonds (Chrenko, 1973), is a highly

mobile element in aqueous fluids and exhibits incompatible behavior during partial melting. It is concentrated in oceanic sediments (1-100 ppm), hydrothermally-altered oceanic crust (9-70 ppm), as well as serpentinite (10-90ppm) and is often considered to be an indicator of slab contribution to island-arc melts (e.g., De Hoog and Savov, 2018).

Type IIb blue diamonds are very rare, constituting only ≤ 0.02% of the diamonds extracted worldwide (King et al., 1998; Gaillou et al., 2012). They are found in a few kimberlites from South Africa (Cullinan Mine), Botswana (Orapa and Karowe) and – of uncertain origin – from alluvial deposits in India (Kollur Mine). They are very expensive on the diamond market and therefore not readily available for research, as demonstrated by the scarcity of published studies (King et al., 1998; Gaillou et al., 2012; Smith et al., 2018a and b). Recently, based on inclusions of majorite, jeffbenite and bridgmanite trapped in a series of type IIb diamonds, Smith et al. (2018a) proposed that blue diamonds are sublithospheric and originate within either the transition zone or the lower mantle, in relation to subduction settings.

Here, a collection of forty-nine type IIb diamonds extracted from the Cullinan Mine (formerly Premier Mine), South Africa, was studied. Five of these diamonds contain single or multi-phased inclusions and thus they were the focus of this study. Among these, five inclusion-bearing diamonds were studied with a combination of non-destructive in-situ methods to preserve the gems and avoid loss of the inclusions, with the aim of identifying their parent fluids and their growth conditions. Further, this study addresses why these type IIb diamonds contain both no nitrogen and very little boron, and discusses the appropriateness of linking boron-bearing diamonds to boron-rich environments, such as subduction zones.

## 2. Materials and Methods

*2.1 Geological background and samples*

The Cullinan kimberlite is located in the Gauteng Province, 130 km north-east of Johannesburg, in the center of the Kaapvaal craton, one of the oldest fragments of continental lithosphere of Archean age (Fig. 1). The crystallization ages of the Kaapvaal crust range from 3.6 to 2.6 Ga, and its mantle root – made up of highly-depleted mantle peridotites of dunite/harzburgite composition (Viljoen et al., 2004) – is as old as 3.5 Ga (Moser et al., 2001). The region became a stable continental plate at 3.0 Ga (Moser et al., 2001) and successively underwent one of the oldest recognized episodes of plate subduction 2.93-2.88 Ga ago (Schmitz et al., 2004). The Kaapvaal craton was intruded by repeated injections of magma, which gave rise to the layered structure of the Bushveld Complex at 2.05 Ga, refertilizing the lithosphere by melt-related metasomatic processes. The Cullinan kimberlite emplaced through the ultramafic-to-mafic rocks of the Bushveld Complex (Allsopp et al., 1989) at 1.18±0.30 Ga (Scoates and Friedman, 2008). This deposit is well-known for its large, colorless diamonds, such as the largest gem-quality rough diamond ever found, the Cullinan (3106 carats rough crystal), as well as its blue diamonds, such as the Cullinan Dream (24.18 ct fancy blue cut from a 122.5-ct rough).

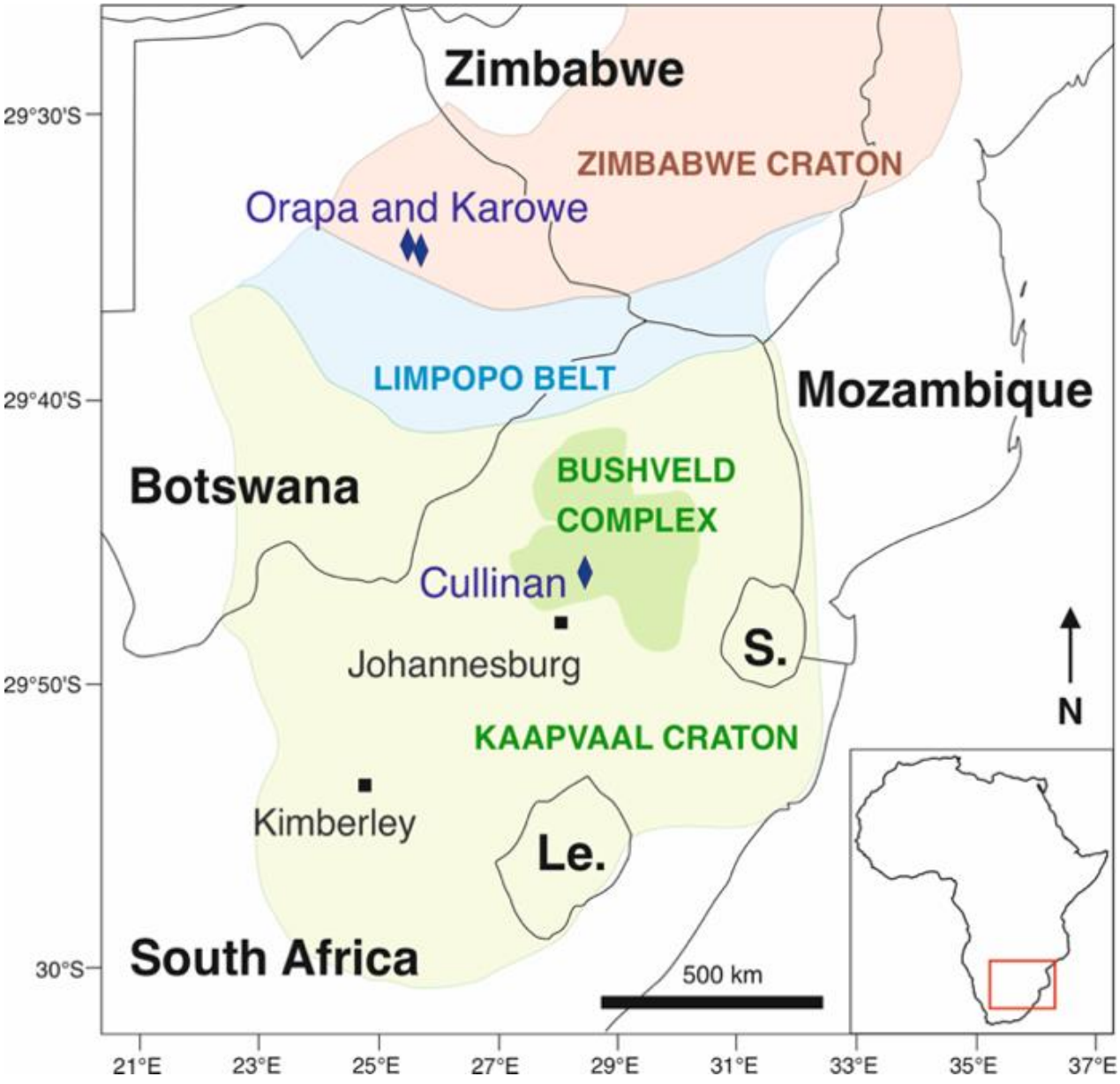


***Figure 1***. *Simplified geological map of South Africa, with the Kaapvaal and the Zimbabwe cratons of Archean age. Blue diamond symbols indicate type IIb diamond mines. Abbreviations: Le.=Lesotho; S.=Swaziland.*

Previous investigations revealed that most of the diamonds from the Cullinan Mine are of lithospheric origin (Deines et al., 1989; Thomassot et al., 2007), while Moore and Helmstaedt (2019) identified a bimodal population: 1) a Mg-rich suite (basic to ultrabasic, corresponding to sublithospheric diamonds; and 2) a Ca-rich suite (including breyite) linked to the websteritic suite

and thus of lithospheric provenance. A few specimens are sublithospheric, as inferred from the discovery of a perovskite-structured polymorph of $CaSiO_3$ (Nestola et al., 2018). In a detailed study of inclusions trapped in exceptional gem diamonds from Letseng mine (Lesotho), Smith et al. (2016) proposed a model involving crystallization from a redox-sensitive metallic liquid phase in the deep mantle. These large gems, referred to as CLIPPIR (for Cullinan-Like, Inclusion-Poor, relatively Pure, Irregularly shaped and Resorbed), contain inclusions of solidified Fe-Ni-C-S melt, wrapped in a thin fluid layer of $CH_4 \pm H_2$ that would involve a subduction-related formation under metal-saturated conditions.

In the present study, a set of forty-nine type IIb diamonds from the Cullinan Mine production were selected and donated when the mine was still owned by De Beers (Fig. 2). The forty-nine diamonds are broken fragments from larger original crystals, faint-to-fancy blue in color, ranging from 1.5 to 5 mm in diameter with a similar rounded, irregular appearance. Despite being fragments, the presence of cleaved surfaces, conchoidal-to-irregular fractures and growth marks on thirty-two of the forty-nine specimens allowed in-situ measurements such as micro-FTIR, which revealed measurable amounts of uncompensated boron, confirming their type IIb nature. The irregular and rough surfaces of the remaining seventeen specimens made measurement of their boron content impossible. The detailed description of the totality of specimens is reported in Table 1.

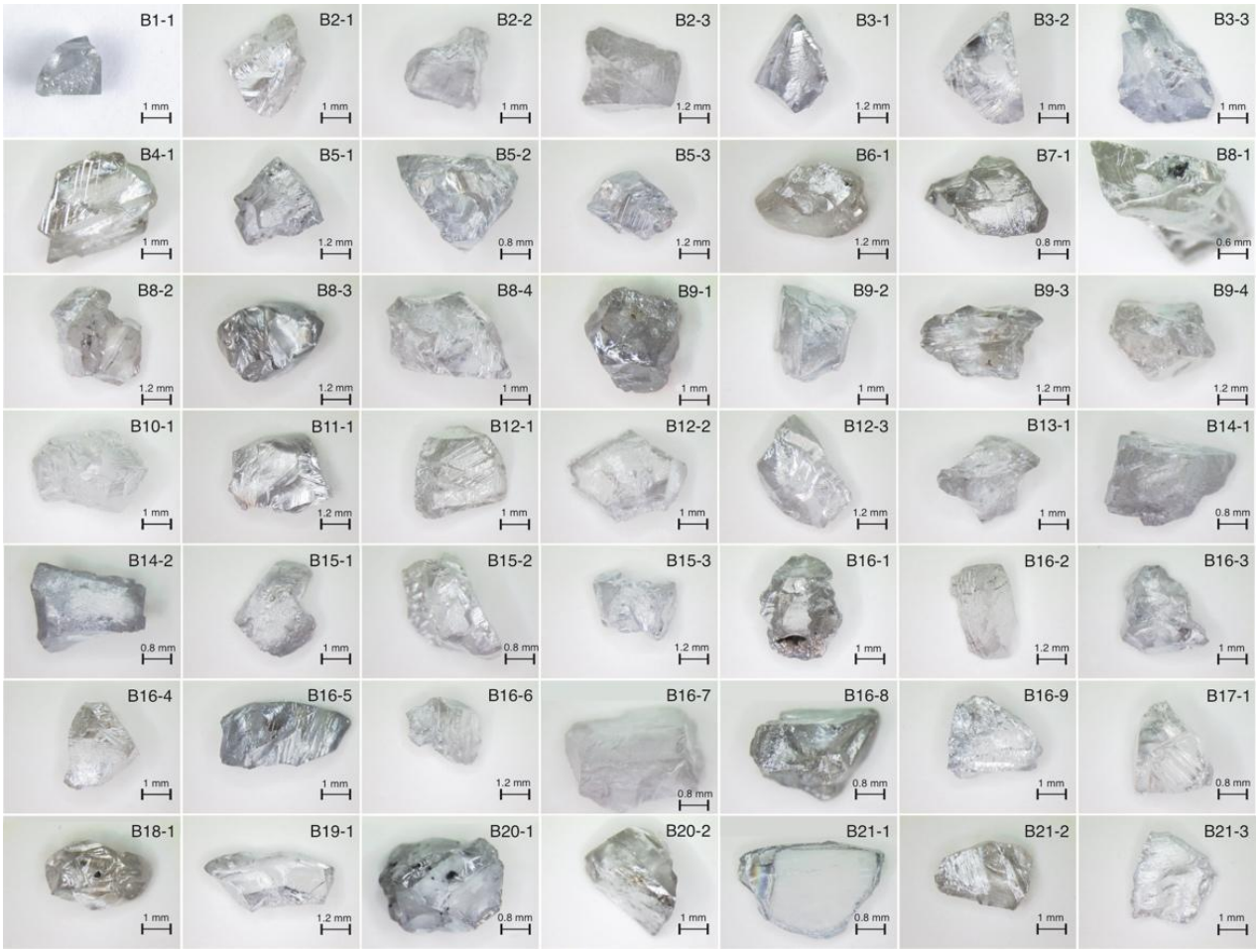


***Figure 2.*** *Photographs of the forty-nine type IIb diamonds donated by De Beers group from the Cullinan Mine.*

**Table 1.** Summary of the FTIR, micro-Raman and SXRD measurements as well as inclusion descriptions of the studied type IIb diamonds.

| Name | Weight (ct) | Size (mm) | Description | Inclusion type | FTIR (B ppm) | Raman[1] | SXRD | XRF | SEM-EDX |
|---|---|---|---|---|---|---|---|---|---|
| B1-1 | 0.27 | | Fancy light blue crystal with an irregular shape and a fracture | None | NM | nm | nm | nm | nm |
| B2-1 | | 2.5 × 2.5 | Faint blue crystal with an irregular shape and conchoidal fractures | None | NM | nm | nm | nm | nm |
| B2-2 | 0.52 | 2.5 × 2 | Faint blue crystal with an irregular shape | None | NM | nm | nm | nm | nm |
| B2-3 | | 3.6 × 2.4 | Faint blue crystal with an irregular shape and growth marks on the surface | None | NM | nm | nm | nm | nm |
| B3-1 | | 4.2 × 2.4 | Light blue crystal with an irregular shape and growth marks on the surface | Primary: black, flat dendritic inclusions | NM | NM[2] | nm | nm | nm |
| B3-2 | 0.40 | 4.8 × 3.12 | Light blue crystal with an irregular shape and several cleaved surfaces | None | 0.08 | nm | nm | nm | nm |
| B3-3 | | 4.5 × 3 | Fancy light blue crystal with an irregular shape, a cleaved surface and iridescent colors in a fracture | None | 0.61 | nm | nm | nm | nm |
| B4-1 | 0.23 | 4 × 2 | Faint blue macle, growth marks on the surface and iridescent colors in a fracture | Primary: small black inclusion | 0.29 | nm | nm | nm | nm |
| B5-1 | 0.60 | 2.4 × 3.48 | Fancy light blue crystal with an irregular shape | Primary and Secondary: small black inclusions close to the surface | NM | NM | nm | nm | nm |
| B5-2 | | 3.2 × 2.4 | Fancy light blue crystal with an irregular shape and a cleaved surface | Primary: small black inclusions | NM | nm | nm | nm | nm |

| | | | | | | | | | |
|---|---|---|---|---|---|---|---|---|---|
| B5-3 | | 3.24 × 2.4 | Fancy light blue macle, growth marks on the surface and broken surfaces | None | 0.29 | nm | nm | nm | nm |
| B6-1 | 0.28 | 3.2 × 1.6 | Faint blue crystal with an irregular shape, conchoidal fractures and iridescent colors in a fracture | Primary: black and colorless inclusions | NM | Graphite, breyite, larnite | nm | Fe-Ni-Cu alloy | nm |
| B7-1 | 0.26 | 2.96 × 2 | Faint blue crystal with an irregular shape, growth marks on the surface and conchoidal fractures | None | 0.39 | nm | nm | nm | nm |
| B8-1 | | 1.5 × 2.4 | Light blue crystal with an irregular shape, a cleaved surface and growth marks on the surface | Primary and Secondary: cubo-octahedral shaped mineral inside a circular inclusion in healed fractures, and black inclusions | 0.22 | Graphite, $H_2O$, methane | Graphite, *fcc*-(Ni,Fe), *bcc*-(Fe,Ni), | Fe-Ni alloy | nm |
| B8-2 | 0.93 | 2.04 × 3.6 | Light blue crystal with an irregular shape, and a cleaved surface | Primary: black inclusions | 0.23 | Graphite | nm | nm | nm |
| B8-3 | | 4.2 × 3 | Light blue-gray crystal with an irregular shape | Primary: small black inclusions | 0.35 | NM | nm | nm | nm |
| B8-4 | | 4.5 × 3 | Faint blue crystal with an irregular shape and a cleaved surface | None | 0.23 | nm | nm | nm | nm |
| B9-1 | | 3 × 3 | Light blue-gray crystal with an irregular shape and growth marks on the surface | Primary: small black inclusions | 0.23 | NM | nm | nm | nm |
| B9-2 | 0.73 | 3 × 2 | Fancy light blue macle, several cleaved surfaces and growth marks on the surface | Primary: small black inclusions | NM | nm | nm | nm | nm |
| B9-3 | | 3.6 × 2.4 | Faint blue crystal with an irregular shape and growth marks on the surface | Primary: small black inclusions | 0.12 | nm | nm | nm | nm |
| B9-4 | | 2.4 × 3.6 | Faint blue crystal with an irregular shape and growth marks on the surface | Primary: small black inclusions | 0.34 | nm | nm | nm | nm |
| B10-1 | 0.20 | 4 × 2 | Faint blue crystal with an irregular shape and growth marks on the surface | None | NM | nm | nm | nm | nm |
| B11-1 | 0.22 | 4.2 × 2.4 | Faint blue-gray crystal with an irregular shape and growth marks on the surface | Primary: small black inclusions | 0.17 | NM | nm | nm | nm |

| | | | | | | | | | |
|---|---|---|---|---|---|---|---|---|---|
| B12-1 | 0.37 | 2.3 × 2.2 | Faint blue crystal with an irregular shape and growth marks on the surface | Primary: small black inclusions | 0.29 | nm | nm | nm | nm |
| B12-2 | | 2.7 × 4 | Faint blue crystal with an irregular shape, growth marks on the surface and iridescent colors in a fracture | None | 0.13 | nm | nm | nm | nm |
| B12-3 | | 4.2 × 2.4 | Fancy light blue crystal with an irregular shape | Primary: small black inclusions | 0.24 | nm | nm | nm | nm |
| B13-1 | 0.12 | 3.5 × 1.5 | Fancy light blue crystal with an irregular shape | Primary: small black inclusions | NM | nm | nm | nm | nm |
| B14-1 | 0.20 | 3.2 × 2.16 | Fancy light blue crystal with an irregular shape | None | 0.28 | nm | nm | nm | nm |
| B14-2 | | 3.6 × 1.6 | Fancy blue crystal with an irregular shape | None | 0.43 | nm | nm | nm | nm |
| B15-1 | | 3 × 3.2 | Fancy light blue crystal with an irregular shape | None | NM | nm | nm | nm | nm |
| B15-2 | 0.36 | 1.2 × 3.6 | Faint blue crystal with an irregular shape and growth marks on the surface | None | NM | nm | nm | nm | nm |
| B15-3 | | 3.6 × 2.4 | Fancy light blue crystal with an irregular shape | None | 0.32 | nm | nm | nm | nm |
| B16-1 | | 4 × 3 | Fancy blue crystal with an irregular shape, a cleaved surface, growth marks on the surface and iridescent colors in a fracture | Primary: black inclusions and Secondary: black cubo-octahedral shaped mineral inside a circular inclusion in healed fractures | 0.38 | Graphite, $H_2O$, methane | Graphite, (Fe,Ni)O | Fe-Ni-Cu alloy | NiO, (Ni,Fe) alloys, pyrrhotite |
| B16-2 | | 4.44 × 2.4 | Faint blue crystal with an irregular shape and a cleaved surface | Primary: small black inclusions | NM | NM | nm | | nm |
| B16-3 | 1.10 | 3 × 2.4 | Fancy blue crystal with an irregular shape | None | NM | NM | | | |
| B16-4 | | 3.2 × 2.8 | Faint blue crystal with an irregular shape | None | 0.19 | nm | nm | nm | nm |
| B16-5 | | 5 × 2.5 | Fancy blue crystal with an irregular shape and a cleaved surface | Primary: small black inclusions | 0.54 | nm | nm | nm | nm |
| B16-6 | | 3.6 × 2.4 | Light fancy blue crystal with an irregular shape | None | NM | | | | |

| | | | | | | | | | |
|---|---|---|---|---|---|---|---|---|---|
| B16-7 | | 3.52 × 4.2 | Light fancy blue crystal with an irregular shape and iridescent colors in a fracture | None | 0.08 | nm | nm | nm | nm |
| B16-8 | | 4 × 1.6 | Fancy blue-gray crystal with an irregular shape and a cleaved surface | None | NM | | | | |
| B16-9 | | 3 × 3 | Light fancy blue crystal with an irregular shape and iridescent colors in a fracture | None | 0.30 | nm | nm | nm | nm |
| B17-1 | 0.07 | 2.88 × 2.4 | Faint blue crystal with an irregular shape and growth marks on the surface | None | 0.04 | nm | nm | nm | nm |
| B18-1 | 0.13 | 2.7 × 4 | Faint blue-gray crystal with an irregular shape and growth marks on the surface | Primary: black inclusions | NM | Graphite, $H_2O$, methane | nm | | nm |
| B19-1 | 0.17 | 5.64 × 2.4 | Faint blue-gray crystal with an irregular shape and a cleaved surface | None | 0.32 | nm | nm | nm | nm |
| B20-1 | 0.31 | 2.4 × 3.36 | Fancy blue crystal with an irregular shape and conchoidal fractures | Primary: small and large black inclusions | 0.31 | Graphite, O-H, breyite, larnite, ferricopiapite | Graphite, breyite, *bcc*- (Fe,Ni), *fcc*-(Ni,Fe) | Fe-Ni-Cu alloy | nm |
| B20-2 | | 2 × 3.5 | Light fancy blue-gray crystal with an irregular shape and a cleaved surface | Primary: small black inclusions | NM | NM | nm | nm | nm |
| B21-1 | | 4.56 × 2.96 | Light fancy blue crystal with a flat shape, a cleaved surface and iridescent colors in a fracture | Primary: small black inclusions | 0.19 | NM | nm | nm | nm |
| B21-2 | 0.22 | 2.5 × 3.6 | Light fancy blue-gray crystal with an irregular shape and growth marks | Primary and Secondary: small black inclusions | 0.09 | NM | nm | nm | nm |
| B21-3 | | 3.2 × 3.1 | Light fancy blue crystal with an irregular shape and a cleaved surface | None | 0.25 | nm | nm | nm | nm |

1: measured if contains inclusions; NM: not measurable in situ; nm: not measured

Twenty-four of the forty-nine diamonds display either single phase or multiple phase inclusions, including both solids and fluids. Among them, five diamonds (samples B6-1, B8-1, B16-1, B18-1 and B20-1) exhibit measurable inclusions with non-destructive techniques such as FTIR and micro-Raman spectroscopy (Fig. 3). These five samples were studied in situ, to prevent any irreversible damage on the inclusions, except for specimen B16-1 which had been selected to expose a part of its inclusions.

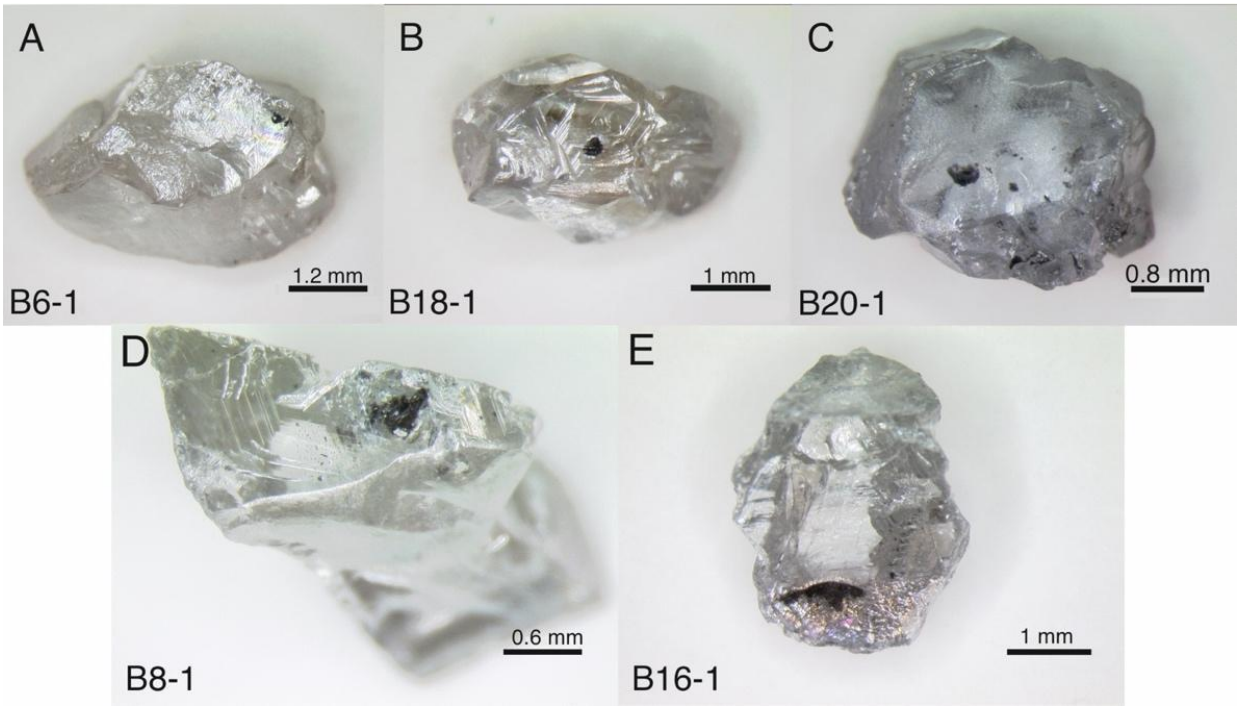


***Figure 3****. Photographs of the five type IIb diamonds containing multi-phased mineral inclusions selected for this study: (A) sample B6-1, (B) sample B18-1, (C) sample B20-1, (D) sample B8-1 and (E) sample B16-1.*

## 2.2 Methods

### *2.2.1 Cryo ion-beam milling*

To obtain one mirror-polished section and to preserve the inclusions from tearing, sample B16-1 was exposed using ionic argon cryo-polishing, performed under high vacuum and at -100˚C.

A Leica EM TIC 3X Ion Beam Milling System device was used, which allows perfect polishing using three broad argon ion beams. The three ion beams intersect at the edge of a tungsten carbide mask, which partially hides the sample. The area of the sample that is exposed to the beams (100µm from the edge) was sputtered at 10kV, 3.5mA. The diamond milling rate is almost 10 times lower than the Si milling rate at 10 kV (300µm/h with $Ar^+$).

*2.2.2 Micro-FTIR spectroscopy*

To determine the uncompensated boron concentration, Fourier Transform InfraRed (FTIR) spectroscopy measurements were performed on the forty-nine specimens (Table 1; Fig. 4). A Bruker IFS 66v/s FTIR spectrometer, equipped with a continuum infrared microscope with a 32 × transmission/reflection objective and an aperture of 250 × 250 µm, was used at the *Institut de Minéralogie, de Physique des Matériaux et de Cosmochimie* (IMPMC), Sorbonne Université. Absorbance was measured at the maximum light transmission for 72 s over a spectral range of 600 to 6000 $cm^{-1}$ and a spectral resolution of 4 $cm^{-1}$, with 128 scans accumulated for each spectrum. Background spectra were collected for 72 s before analyses and are subtracted from each measured absorbance spectrum. Diamond spectra were normalized to 12.2 Au (absorbance units) at 1994 $cm^{-1}$ wavenumbers to convert from absorbance to absorption coefficient values (Collins, 1982). Boron concentration was determined in thirty-two of the forty-nine samples (Table 1) at 2800 $cm^{-1}$ using an absorption coefficient of 0.035 ppm $cm^{-1}$ to obtain the uncompensated boron content in atomic ppm (Fisher et al., 2009).

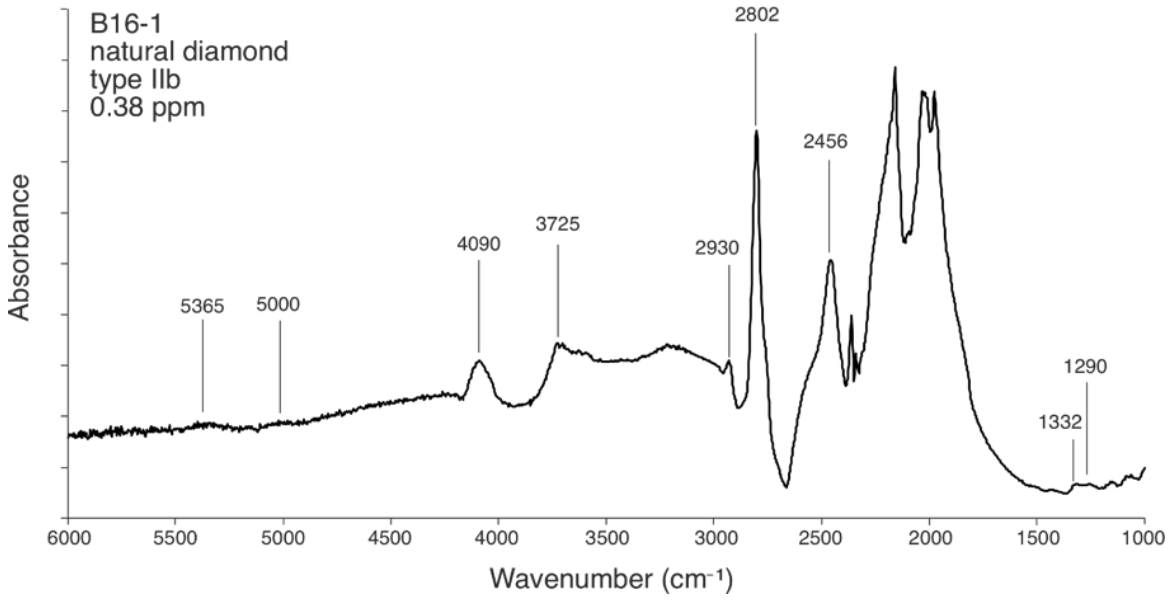


***Figure 4.*** *FTIR spectra of sample B16-1. Typical boron-related bands are labeled on the spectrum with their wavelength values. The boron concentration of 0.38 ppm is calculated using FTIR spectra normalization at 1994 cm$^{-1}$, with y = 12.2 Au (absorbance/cm).*

### *2.2.3 Micro-Raman spectroscopy*

Confocal micro-Raman spectroscopy measurements were performed in situ on all accessible inclusions trapped in the diamonds to identify their nature. The samples were analyzed using a micro-Raman Invia Renishaw spectrometer at the *Centre de Recherche sur la Conservation of the Muséum National d'Histoire Naturelle*, Paris. A 532 nm wavelength excitation laser beam of a 2 μm size was used for inclusion characterization, with scales ranging between 900 cm$^{-1}$ and 3600 cm$^{-1}$ at a power of less than 10% (corresponding to 8.5 mW on the sample at a magnification of 20 ×) to avoid any damage to the inclusions. Additionally, spectra were baseline corrected. Micro-Raman spectral imaging was performed on one inclusion with a high power of 50% (8.5 mW) on large areas of 20 × 20 μm.

### *2.2.4 Scanning electron microscopy*

Scanning electron microscopy was performed at the IMPMC using a SEM-FEG Zeiss electron microscope. Imagery was performed on two bulk specimens (B16-1 and B8-1) using a voltage of 2 kV. Quantitative chemical analyses at the surface of the polished section of diamond B16-1 were obtained by energy dispersive X-ray (EDX) analysis, with a voltage of 15 kV using international standards (Astimex Standards Ltd.) as calibrants.

*2.2.5 X-ray diffraction*

X-ray diffraction (XRD) patterns were collected in situ on inclusions trapped in diamonds using the micro X-ray diffractometer installed at the *Pression Structure Imagerie par Contraste à Haute Énergie* (PSICHÉ) beamline of the SOLEIL synchrotron facility in Saclay, France. A monochromatic (33 keV) micro-focused beam (15 × 20 μm VxH) was used. Inclusion-bearing diamonds were fixed on copper pinholes to facilitate pre-alignment in the X-ray beam. The inclusions were then optically-aligned on the vertical rotation axis of the goniometer using the high-resolution objectives available on the beamline. Diamond refraction was further minimized by selecting only those inclusions very close to the surface (46 inclusions). This protocol allowed for the collection of data on large angle ranges (±20˚), both increasing statistics while minimizing the effect of phase-preferential orientation inside the inclusions. Complementary in-situ XRD was performed at IMPMC, using a RIGAKU MM007HF Mo rotating anode X-ray diffractometer (17.48 KeV; wavelength of 0.7093 Å) equipped with Elliptical CMF/VariMax optics and a double image plate Raxis IV++ detector (300 × 300 mm, $1x10^6$:1 photons/pixel, 100 × 100 μm). This configuration allowed for a beam size of 200 μm at the surface of the sample. Data analysis was performed using DIOPTAS software (Prescher and Prakapenka, 2015) to obtain 2D projections and GSAS software (Toby, 2001) to identify the phases.

### *2.2.6 X-ray fluorescence*

X-ray fluorescence (XRF) analyses were carried out in situ on several dozen inclusions trapped close to the surface of the diamonds at the *Laboratoire Archéomatériaux et Prévision de l'Altération* of CEA-Saclay, France. A high-flux X-ray generator, equipped with a XENOCS® FOX2D MO 25-25P multilayer mirror with a Mo source at 17.48 keV (Mo-Ka), was used to generate a monochromatic X-ray beam of 30 × 50 μm, with a flux of ca. 1 Mph/s. XRF spectra were collected through a Ketek AXAS Vitus Si-drift detector (SDD – 10 $mm^2$ of active area) in reflection geometry. In-situ measurements of inclusions in the diamonds were monitored by a camera equipped with a focusing zoom. The strong absorption of fluorescence due to the thickness of the diamonds between the inclusions and the detector compromised the measurements of low-energy elements such as S, Si, K, Na and Ca, therefore allowing detection only above 6 KeV (i.e., Fe, Ni, Cu...). Semi-quantitative chemical analyses were carried out in situ on a few dozen inclusions trapped close to the surface of the diamonds.

## 3. Results

### *3.1 Boron contents*

Boron concentration determined by FTIR spectroscopy ranged from 0.04 at.ppm to 0.61 at.ppm with a median value of 0.27 at.ppm (Table 1). It is worth remembering that only the uncompensated boron concentration (i.e., boron not compensated by another atom, usually nitrogen) can be measured using this method, which represents a lower limit for the real boron content in diamonds (Gaillou et al., 2012). As expected for type IIb diamonds, no nitrogen was detected by FTIR.

### *3.2.Mineralogical description of the inclusions*

#### *3.2.1.Primary inclusions*

Primary inclusions are defined as trapped during the growth of the host crystal (Roedder, 1979). These inclusions are therefore isolated inside the crystal, totally surrounded by the diamond without any connection to either the exterior or to another inclusion. They are therefore contemporaneous to or predate the formation of the diamond (i.e., syngenetic or protogenetic, respectively). Primary inclusions were found in B6-1, B16-1, B18-1 and B20-1 (Table 1). They occur as a single phase or as an association of multiple phases, forming isolated bodies, which are anhedral and more-or-less flat, possibly with a thin envelope of fluid-to-solid mixture (Fig. 5A, B and C). Their size varies from 20 to 500 μm in diameter within the stones. These inclusions provide information about the growth environment, the parent fluids of the diamond and/or the synchronous solid/fluid phases present during its growth.

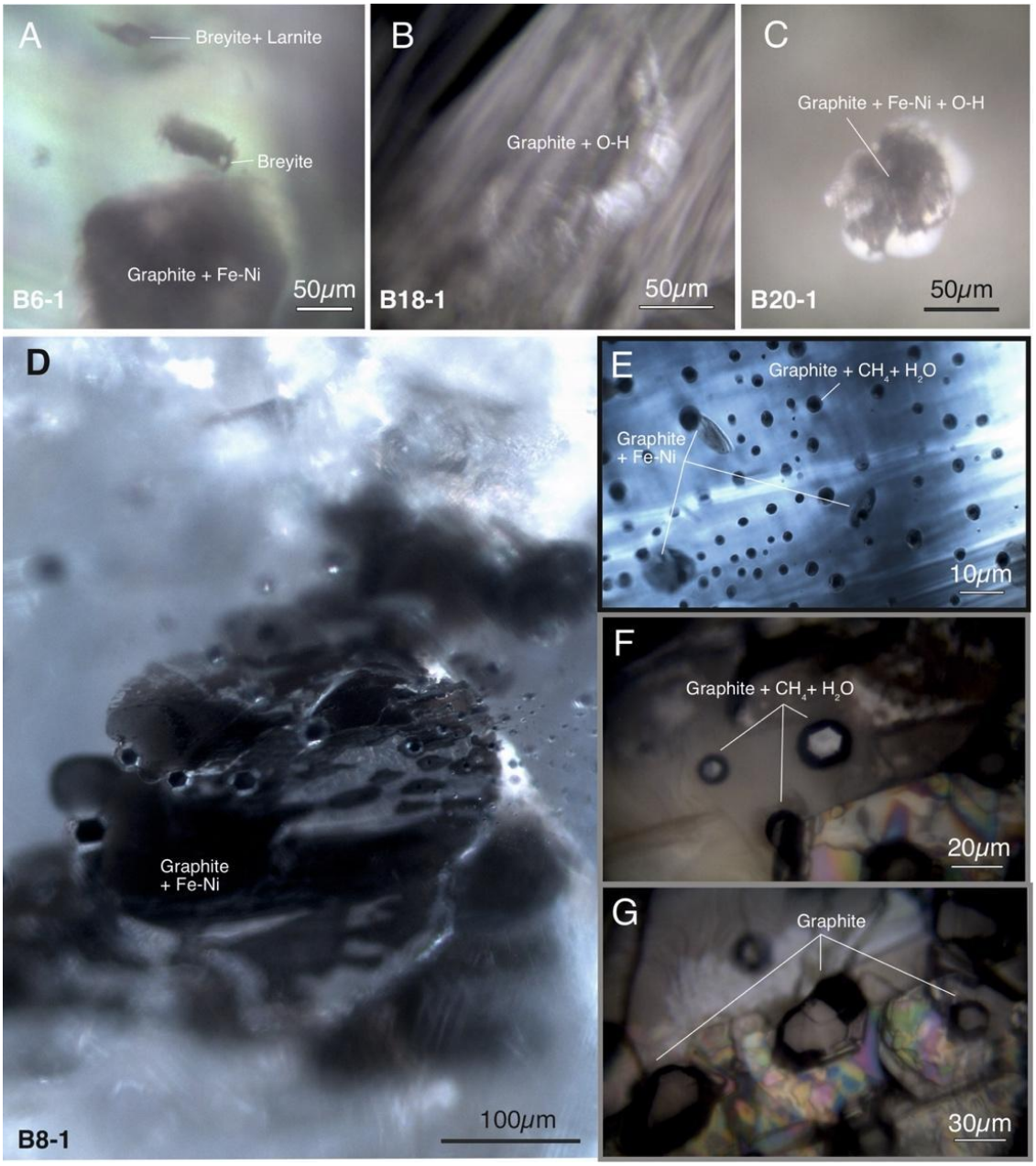


***Figure 5***. *Images of inclusions in the studied diamonds.* ***A)*** *flat primary Fe-Ni-C inclusions in the center, small isolated breyite inclusions located at the bottom left and larnite and breyite inclusions at the top in sample B6-1.* ***B)*** *Primary graphite inclusion, surrounded by a fluid envelope in sample B18-1.* ***C)*** *Primary Fe-Ni and graphite inclusion, surrounded by a fluid envelope in sample B20-1.* ***D)*** *Secondary metallic cluster (Fe-Ni alloys and graphite) in a healed fracture in sample B8-1; small inclusions in front of the cluster are isolated graphite crystals surrounded by a fluid envelope.* ***E)*** *Larger view of the innermost part of the healed fracture in sample B8-1, which exhibits graphite crystals in the center, surrounded by a fluid envelope composed of water and methane (5-15 μm in size) and flat metallic Fe-*

*Ni inclusions of various shapes and a gray hue.* ***F)*** *View of the same healed fracture, but closer to the fracture entrance; inclusions are ~20 μm in size with the same hexagonal graphite crystal in the center, surrounded by a fluid envelope. The healing of the fracture formed small cubo-octahedral-shaped diamonds, the grain boundaries of which connect the inclusions to each other.* ***G)*** *View of the same healed fracture at the fracture entrance. Inclusions exhibit the same graphite crystals (in gray) in the center, but their envelopes follow the morphology of the central graphite. They get larger, up to ~50 μm, and seem to be thicker. The cubo-octahedral diamond crystals healing the fracture are visible in the bottom part of the image, and display iridescent colors likely caused by optical density changes.*

### *3.2.2.Secondary inclusions*

The term "secondary inclusion" is defined as an inclusion trapped by the healing of fractures in the host crystal at some unspecified time after its growth (Roedder, 1979). Secondary inclusions are not isolated, occurring always in association with other inclusions, and postdate the trapping of the primary inclusions. Usually forming within a host crystal's fractures, caused by fluid infiltration, secondary inclusions are possibly associated with protogenetic crystals and also manifest as inclusions aligned along lines or planes after the healing of fractures during a second stage of diamond growth (Fig. 5D). In our samples, they formed suites of inclusions, aligned along planes corresponding to the healing of the fractures by a second generation of diamond material and are associated with large dark inclusions (Figs. 5D-G and 6). This alignment is consistent with a melt trapped along a crystalline plane.

Diamonds B8-1 and B16-1 exhibit similar secondary healed fractures. In both cases, the outer part of the fracture displays iridescence, though this does not extend to the innermost part of the fracture, indicating that the fracture is completely sealed from the exterior. These fractures are filled with multi-phased inclusions of various compositions and sizes: a mesh of small isolated inclusions (5 to 15 μm), whose sizes increase up to 50 μm close to the edge of the fracture, together with a few isolated small anhedral inclusions (Figs. 5E, F and G and 6); and large (> 300 μm)

clusters with a metallic aspect (Fig. 5D). In sample B8-1, three parallel healed fractures were observed, forming three layers of inclusions along cleavage planes (Fig. 6).

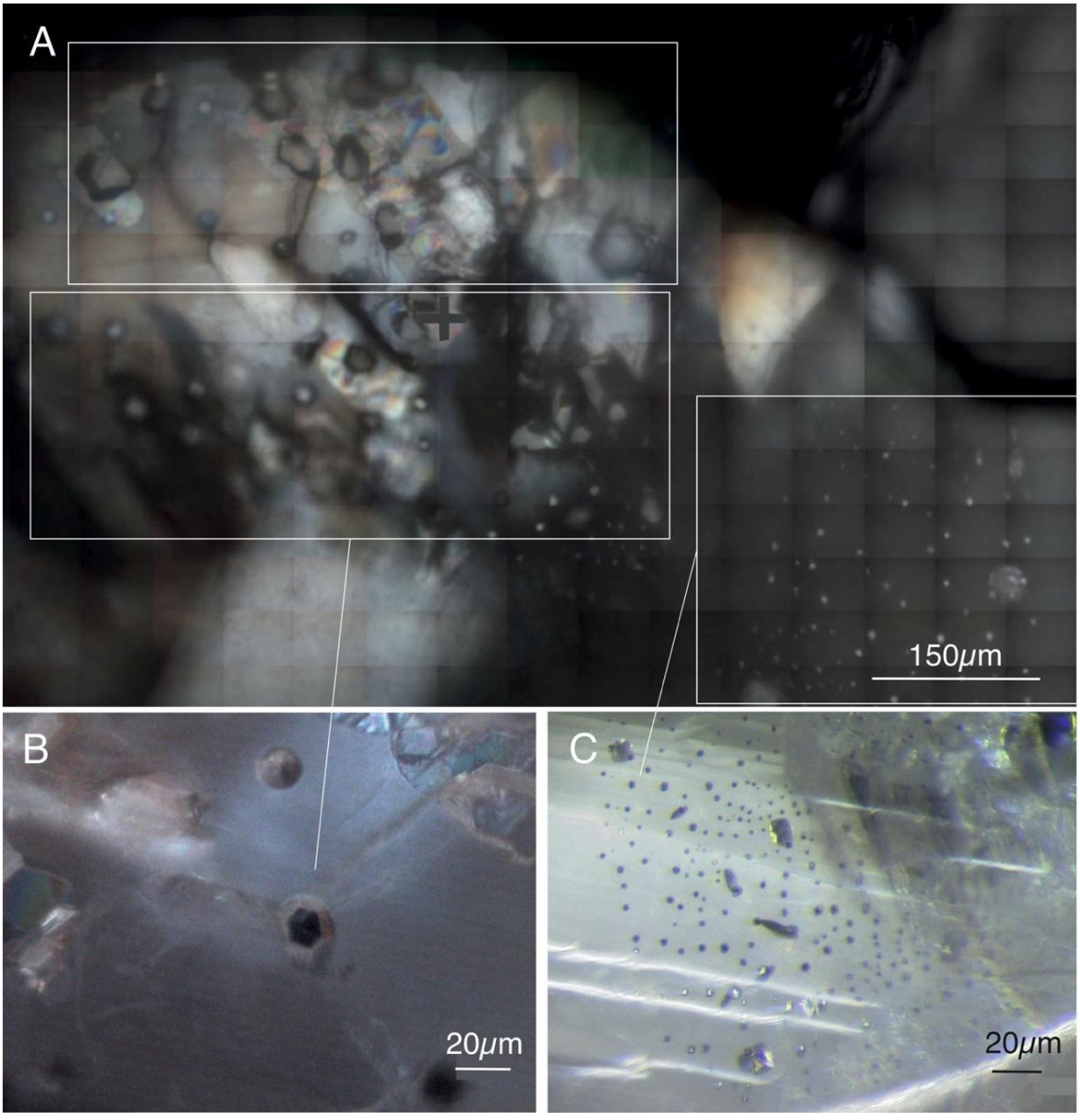


***Figure 6.*** *Images of secondary inclusions trapped in healed fractures of sample B8-1. A) Mosaic view of the entire healed fracture. From bottom to top, highlighted: a group of smaller multi-phased inclusions (5-10 μm size); a group of medium (15-20 μm) to large inclusions (30-50 μm) together in the middle of the healed fracture; a group of larger inclusions (≥50 μm) at the end of the fracture. In the upper rectangle of this picture, central graphite crystals appear.*

*B) Isolated inclusions observed mainly in the middle part of the fracture, formed within an envelope embedded with central graphite crystals. This morphology may be inherited from protogenetic graphite crystals trapped in the inclusions, the latter of which are connected by the grain boundaries between the diamond crystals that have healed the fracture. Some spherical, isolated graphite-free inclusions are also observed.* ***C)*** *View of the inner part of the fracture, composed of isolated inclusions from two populations: multi-phased with central graphite and metallic daughter crystals; and flat metallic inclusions of various shapes. No grain boundaries and no secondary diamond crystals were observed between the inclusions, suggesting the complete healing of the fracture.*

The healed fractures run from the edge of the crystal to ~1 mm inside the crystal (1400 × 800 μm for sample B8-1 and 4500 × 1800 μm for sample B16-1). Healed fractures exhibit distinct zonations from the core to the rim, with a cluster of small, isolated round and flat inclusions observed in the innermost part of the fracture, located in the core of the diamond, associated with shapeless metallic inclusions (Fig. 5E). The size of the inclusions progressively increases (from 5 to > 50 μm) toward the surface (Figs. 5F, G and 6A), associated with a healing process which creates a mosaic of small diamond crystals mimicking the hexagonal shape of graphite. These crystals seem to be connected to each other, forming a network of grain boundaries (Figs. 5F, G and 6B).

Most of the isolated inclusions inside healed fractures show spherical to cubo-octahedral shapes, with the inclusions trapping hexagonal graphite crystals within the fracture (e.g., Fig. 6B). Their sizes range from 5 to 15 μm in diameter in the inner part of the healed fracture, where they are isolated from each other (Figs. 5E and 6C), to < 50 μm in diameter at the limit of the fracture, where they are all connected with the grain boundaries of a small cubo-octahedral shaped diamond network (Fig. 5G). The geometry of the healed fractures and their various inclusions are illustrated in Figs. 5D, G and 6. Inclusions of Fe-Ni alloys and carbon (Fig. 5C-D) have previously been observed in fractures of diamonds with similar appearance (Smith et al., 2017; Shatsky et al.,

2020). However, it is worth noting that, here, no carbides were identified in our samples, with graphite being the main C-bearing phase found in the inclusions instead (Fig. 5C-D).

SEM imaging of the surface of diamonds B8-1 and B16-1 revealed that both diamonds have been fractured and healed (Figs. 7A, B). The composite inclusions (central crystal + envelope) exhibit cubo-octahedral shapes (Figs. 7A, C) and are connected with each other through new diamond crystal grain boundaries. Diamond B8-1 (3 × 2 × 1 mm size) displays growth marks on its surface made of several triangular and six-sided pits, indicating minor resorption of the crystal. Diamond B16-1 ( 3 × 2 × 1 mm size), by contrast, displays a resorbed surface with no visible growth marks. In this case, the euhedral cubo-octahedral shape of the graphite crystals trapped in the so-called secondary inclusions (Fig. 7A) would be more fittingly described as syngenetic (Glinnemann et al., 2003), i.e., trapped together with the fluid rather than formed after the closure of the inclusion, with their shape therefore imposed by the diamond. It is worth noting that diamond B16-1 contains both primary and secondary inclusions crystallized in a subsequent generation of diamond, from which at least two growth episodes can be inferred.

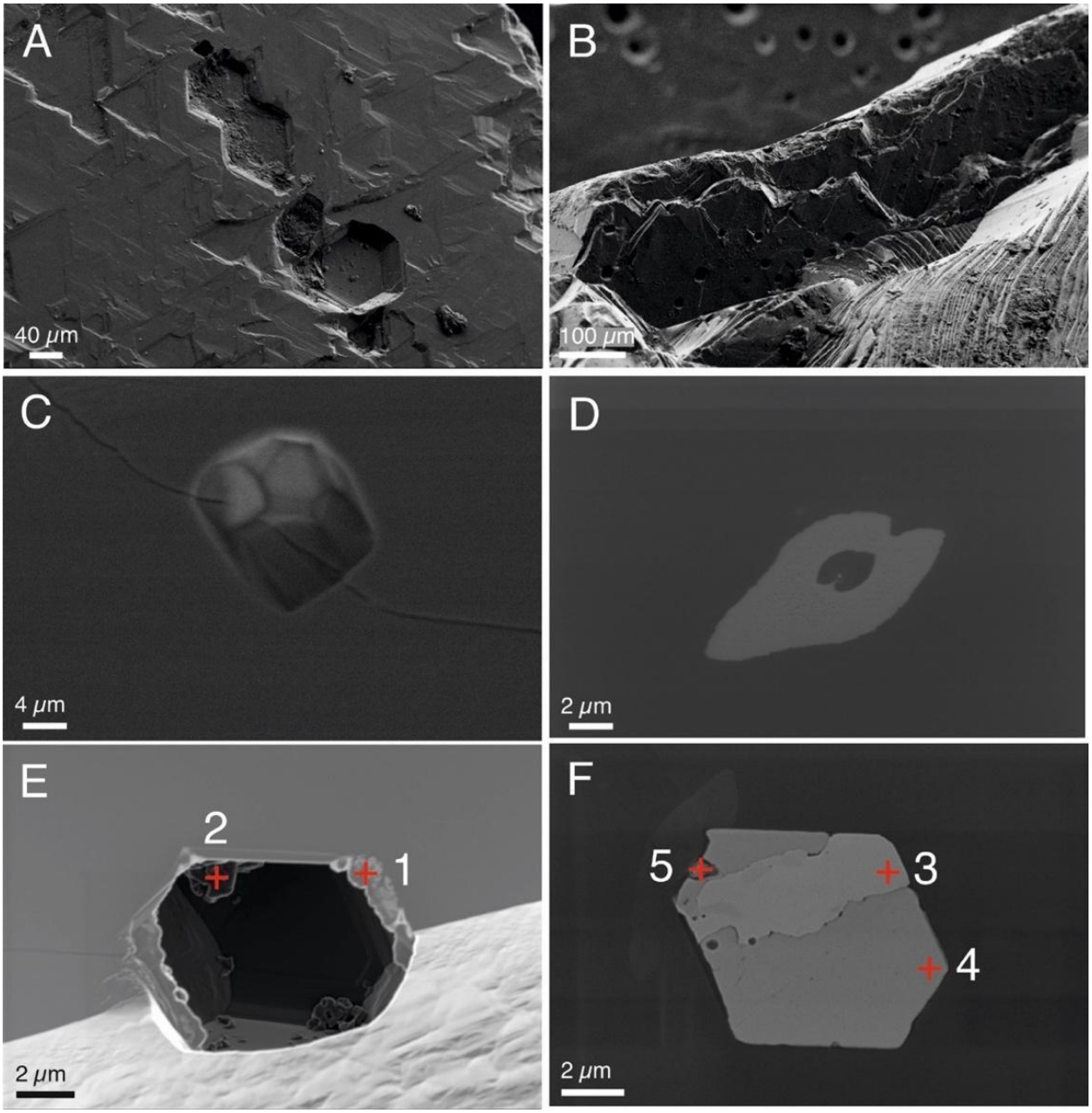


***Figure 7.*** *SEM images of secondary inclusions in diamonds B8-1 and B16-1. A to B: at the diamonds' surfaces (left to right: B8-1 & B16-1), where healed fractures are visible; C to F: diamond B16-1 after experiencing cryo-ionic polishing perpendicular to the fracture.* ***A)*** *The surface of sample B8-1 exhibits triangular and six-sided pits, which correspond to the prints of the now-empty fluid inclusions.* ***B)*** *As with B8-1, sample B16-1's surface displays a resorbed texture.* ***C)*** *Close-up of one inclusion, just below the surface, that is still closed in sample B16-1. A few smaller crystals in the fluid have been observed.* ***D)*** *Close-up of one inclusion that exhibits a large area (in gray) corresponding to the deposition of the residue from the fluid in sample B16-1. The hole from which the fluid escaped*

*is visible at the center of the image, with the deposition forming a small channel and a large elongated area.* ***E)*** *Close-up of one open inclusion from which the fluid is lost in sample B16-1. Small remaining minerals, consisting of almost pure Ni and NiO, as shown by the EDX analyses in Table 2 (red crosses, inclusion 1), are still attached to the walls of the cavity.* ***F)*** *Close-up of one inclusion located in the same healed fracture in sample B16-1, which exhibits three different metallic alloys, as shown by the EDX analyses in Table 2 (red crosses, inclusion 2). The small holes represent the escape of a fluid phase, as indicated by the deposition at the surface on the left of the inclusion.*

### *3.3 Micro-Raman analyses*

#### *3.3.1.Primary inclusions*

In-situ micro-Raman analyses of inclusions allowed for the identification of primary inclusions in samples B-6, B-16, B18-1 and B-20 (see Supplementary Materials, Table 1). The G and 2D (D overtone) modes of graphite (Ferrari, 2007) were identified in five selected diamonds (Figs. 8, 9 and displayed in Fig. 10). They are observed at variable wavenumbers of ~1583-1590 $cm^{-1}$ and ~2726-2740 $cm^{-1}$, with the observed variability being possibly caused by a residual pressure effect. The high intensities of the Raman bands for diamond and graphite (Figs. 8B, D and F) made it difficult to observe other phases, if any were present. Modes in the hydroxyl stretching region (3200-3800 $cm^{-1}$) are also present in all primary inclusions of samples B6-1, B18-1 and B20-1 (Figs. 8B, D, 10A and C), attesting to the presence of aqueous fluid-bearing inclusions.

Three Raman peaks observed at 663, 990 and 1050 $cm^{-1}$ in an isolated inclusion of sample B6-1 (Fig. 8A and 10A) are attributed here to breyite (formerly referred to as $CaSiO_3$-walstromite; Brenker et al., 2020). In another inclusion from sample B6-1, breyite is associated with a different phase that has been identified as larnite, $\beta$-$Ca_2SiO_4$ (Fig. 8C and 10B; Joswig et al., 1999). In sample B20-1, micro-Raman analysis revealed the presence of two inclusions of breyite and larnite

(Fig. 8E), and seven isolated primary inclusions of an unknown hydrous ferric sulfate phase. The Raman spectrum shows strong analogies with ferricopiapite, $Fe^{3+}_{2/3}Fe^{3+}_{4}(SO_4)_6(OH)_2$ $20(H_2O)$ (Figs. 8G, H and 10D), a mineral usually observed as a weathering or $Fe^{3+}$ precipitation product. Further investigations would be required to characterize these hydrous ferric sulfate minerals.

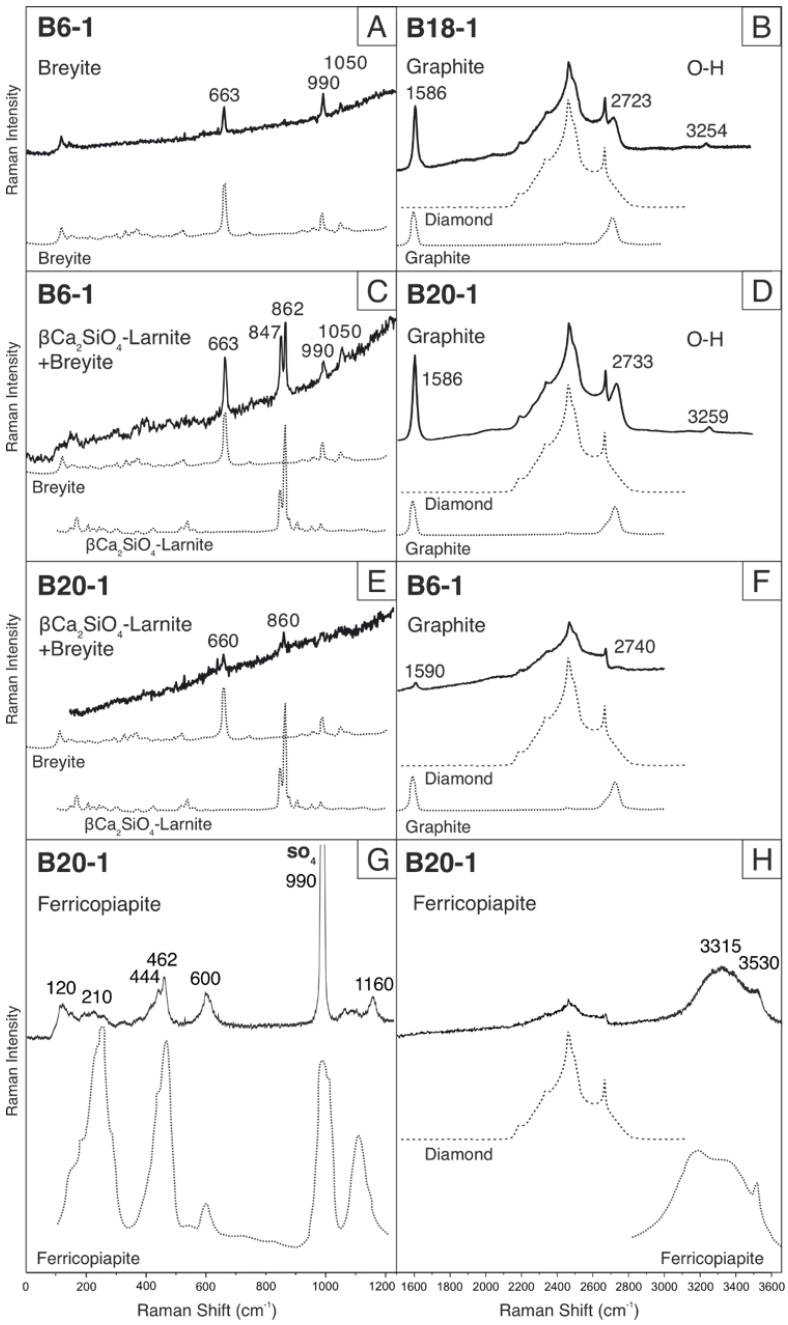

***Figure 8.*** *Raman spectroscopy analysis of primary inclusions.* ***A)*** *Primary isolated inclusion of breyite in sample B6-1. Reference spectra for breyite (dashed line) are from Anzolini et al. (2018).* ***B)*** *Graphite inclusion and water OH in sample B18-1, with graphite and diamond references from the RRUFF database.* ***C)*** *Primary inclusions of breyite and $Ca_2SiO_4$-larnite together in sample B6-1.* ***D)*** *Graphite inclusion, diamond and hydrous species (hydroxyl groups O-H) in sample B20-1.* ***E)*** *Potential presence of primary inclusions of breyite and $Ca_2SiO_4$-larnite in sample B20-1. The poor quality of the Raman spectra is attributed to the depth of the inclusions in the bulk diamond.* ***F)*** *Graphite inclusion and diamond in sample B6-1.* ***G and H)*** *Unknown primary inclusion of a phase very close to a ferricopiapite, with reference taken from the RRUFF database.*

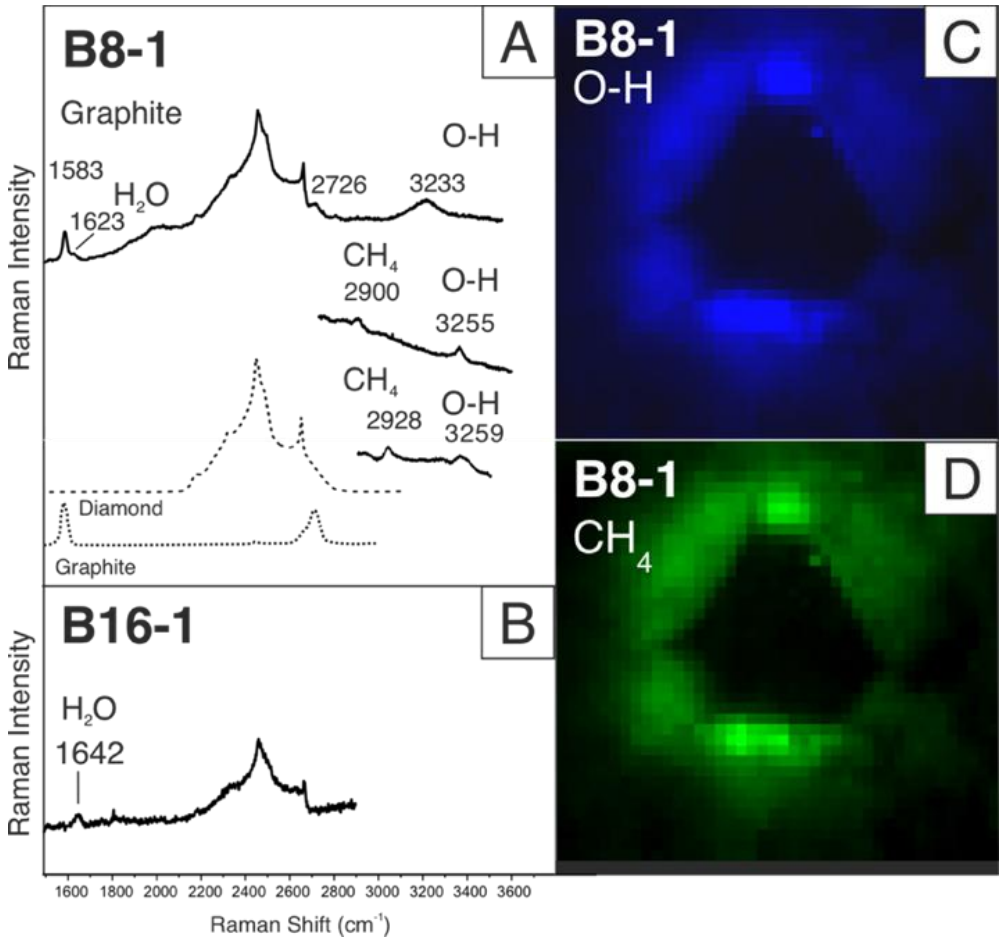


***Figure 9****. Raman spectroscopy analysis of secondary inclusions.* ***A)*** *Graphite and $H_2O$ (O-H stretching and HOH bending modes) measured in the central part of the secondary inclusion in sample B8-1 and* ***B)*** *in sample B16-1. The $H_2O$ signal indicates that the rim (i.e., the envelope surrounding the graphite crystals) is a fluid phase.* ***C)*** *Water O-H Raman mapping of a secondary inclusion in sample B8-1.* ***D)*** *Methane ($CH_4$) Raman mapping of a secondary inclusion in sample B8-1. The high intensity of the graphite signal masks the fluid (OH, $CH_4$) signal at the center of the maps.*

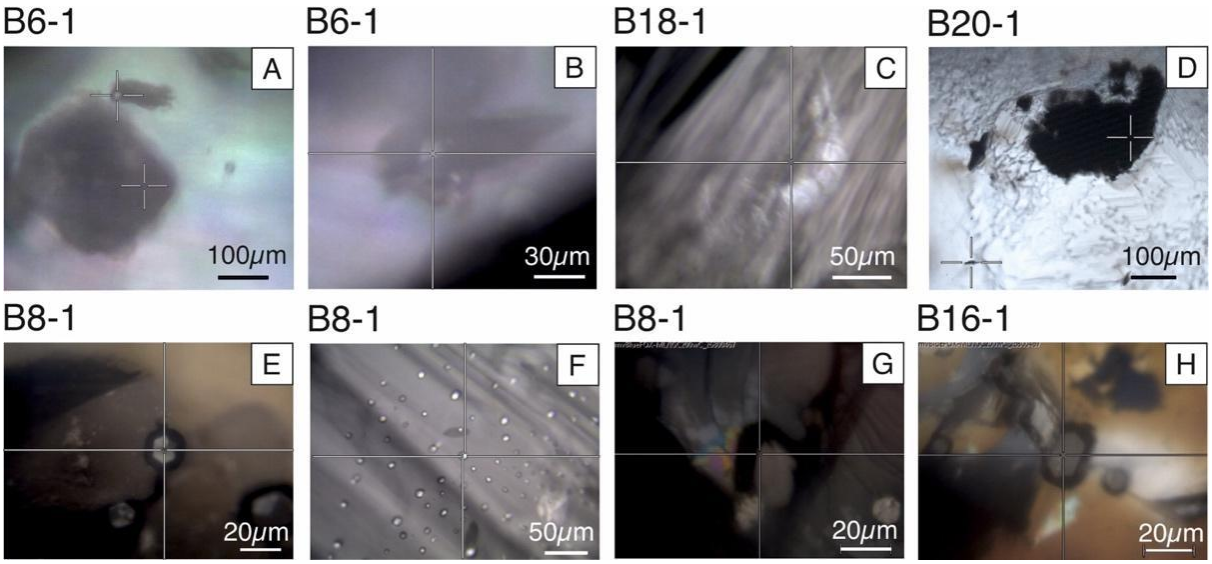


***Figure 10.*** *Images of some of the inclusions analyzed by Raman spectroscopy. The center of the cross indicates the location of analysis.* ***A)*** *Sample B6-1 inclusion of breyite.* ***B)*** *Sample B6-1 inclusion of breyite and $Ca_2SiO_4$-larnite.* ***C)*** *Sample B18-1 cluster of graphite containing a fluid phase.* ***D)*** *One inclusion of ferricopiapite located roughly fifteen micrometers below the surface of diamond B20-1.* ***E, F & G)*** *Secondary inclusions containing water and methane in sample B8-1 and* ***H)*** *in sample B16-1.*

### *3.3.2.Secondary inclusions*

Micro-Raman analyses were performed on the inclusions within the diamond with the main results displayed in Figs. 9 and 10. The multi-phased inclusions consist of central cubo-octahedral crystals identified as graphite (Ferrari, 2007), surrounded by an envelope consisting of small bands related to OH stretching mode from 3255 to 3622 $cm^{-1}$ (Figs. 9A and B), together with water at 1642 $cm^{-1}$ and methane ($CH_4$) at ~2900 $cm^{-1}$ (Figs. 9C and D). Although graphite + methane micro-inclusions were observed previously by Smit et al. (2016) in Marange (Zimbabwe) diamonds, to our knowledge, such multi-phased ($C_{graphite}$, $H_2O$, $CH_4$) and cubo-octahedral-shaped inclusions have never before been reported in any type of natural diamond. This assemblage recalls a high-

pressure hydrous fluid, possibly parented to the diamonds, trapped as primary and secondary inclusions in the crystals.

### *3.4. SEM and EDX analyses*

#### *3.4.1.Secondary inclusions*

Successive cryo-milling perpendicularly crossing the healed fracture in sample B16-1 allowed for the exposure of secondary inclusions composed of different phases (Fig. 7C-F). These phases consist of crystals embedded in a fluid that was subsequently lost upon decrepitation, together with associated minerals (Figs. 7E and F). Fluid loss is inferred from the presence of a layer of residues deposited on the diamond surface (Figs. 7D and E) too thin to be quantitatively analyzed.

A few remaining solid phases are present within the rims of these fluid-bearing inclusions (Fig. 7E; inclusion 1), and depending on the position of the cryo-polishing, large minerals were exposed (Fig. 7F; inclusion 2). SEM-EDX analyses demonstrate that the inclusions contain several metallic alloys (Table 2; inclusions 1 and 2): a Ni-rich oxide containing Fe, Mg, Na, Si and Al (#1) and an almost pure Ni phase associated with Fe, Cr and Si (#2). Isolated inclusions of composite metallic alloys and sulfides also exhibit the same cubo-octahedral shape as graphite crystals characterized by Raman analyses (Figs. 7 E-F). A strong association between graphite layers and these metallic phases in other exposed secondary inclusions was observed. Additionally, a composite inclusion (Table 2: inclusion 2; Fig. 7F) exhibits a layer of a FeNi-rich phase associated with Cu alloy (#3) and a sulfide Fe-S phase with minor Cu (1.49 at%) (#4; pyrrhotite group). The surface of inclusion 2 exposes small cavities most likely initially filled with a fluid (Fig. 7F).

**Table 2.** EDX analyses of two inclusions trapped in the healed fracture of sample B16-1 after the inclusions were exposed by ionic polishing. Analyses are summed to 100. Images of inclusions 1 and 2 are displayed in Figs. 7E and 7F, respectively. Inclusion 1 leaked during diamond opening and contains residual phases. Inclusion 2 contains a sulfide from the pyrrhotite group with Cu and is included in a layer of an alloy composed of Fe, Ni, Cu and a Ni-bearing ferricopiapite.

| Element C (at%) | Fe | Ni | S | Cu | Cr | Si | O | Na | Mg | Al | Ca | K | Total |
|---|---|---|---|---|---|---|---|---|---|---|---|---|---|
| Inclusion 1 | | | | | | | | | | | | | |
| #1 | 2.1 | 44.4 | | | | 2.0 | 39.4 | 6.0 | 4.0 | 1.6 | 0.3 | 0.2 | 100 |
| #2 | 4.1 | 92.2 | | | 1.6 | 2.1 | | | | | | | 100 |
| Inclusion 2 | | | | | | | | | | | | | |
| #3 | 55.6 | 42.0 | | 2.4 | | | | | | | | | 100 |
| #4 | 50.5 | | 48.0 | 1.5 | | | | | | | | | 100 |
| #5 | 42.1 | 15.0 | 16.0 | | | | 26.9 | | | | | | 100 |

### *3.5. X-ray fluorescence of primary and secondary inclusions*

XRF in-situ micro-analyses of near-surface primary and secondary inclusions confirmed the presence of a metallic phase strongly associated with graphite (Fig. 11). Results further confirmed the presence of Fe-Ni-Cu alloys associated with graphite and the hydrous phase detected by micro-Raman spectroscopy and EDX. Metallic alloys are present in both secondary and primary inclusions in four diamonds (B6-1, B8-1, B16-1 and B20-1). Their nature – i.e., metallic alloys or oxides – cannot be determined by using these techniques alone.

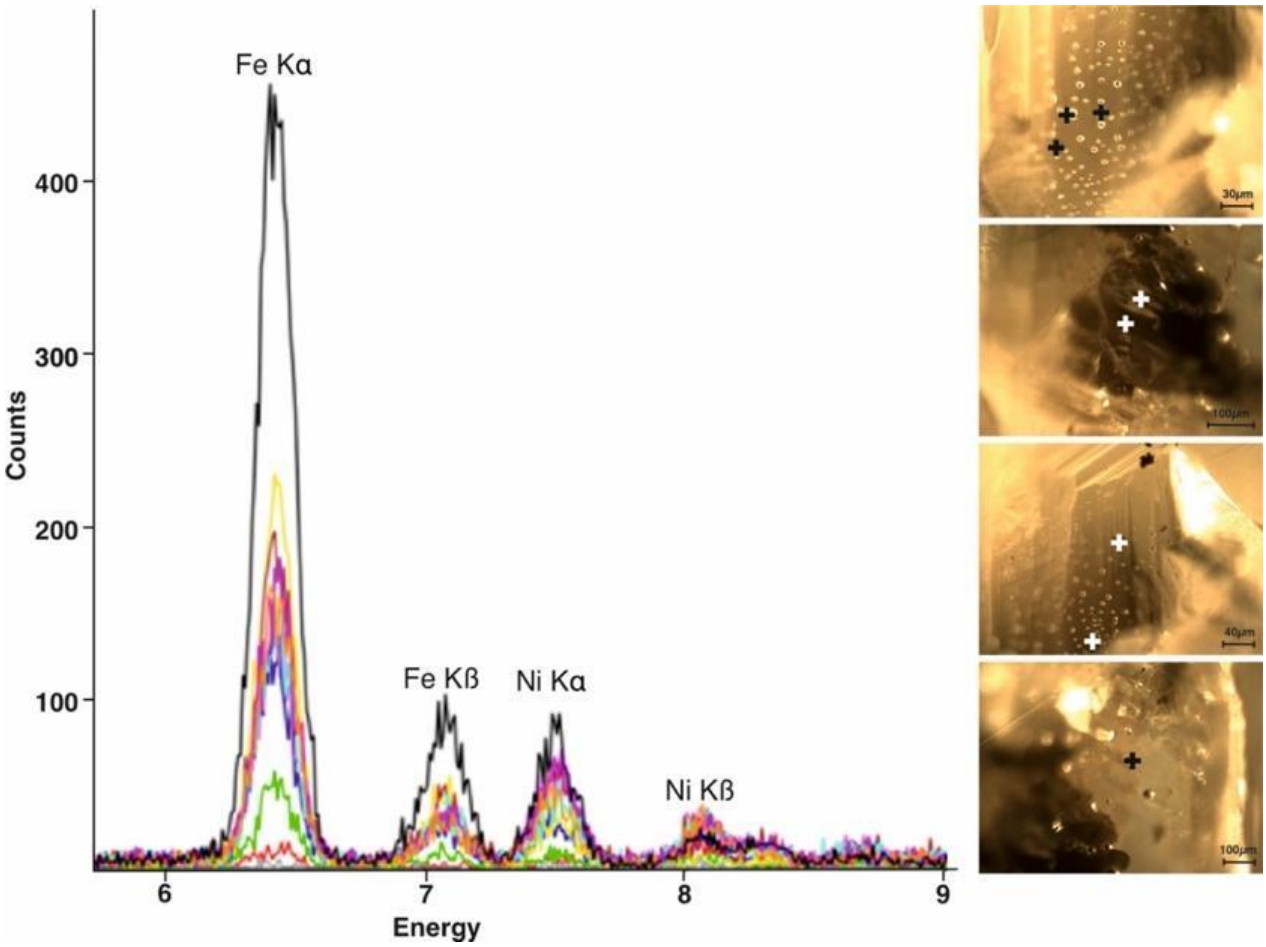


***Figure 11.*** *In-situ X-ray fluorescence measurements performed on inclusions of sample B8-1. Elements are identified thanks to the energy of their K-α and K-ß rays in KeV. Results indicate the presence of Fe-Ni-rich alloys in the cluster and in the isolated inclusions. It is not possible with this analysis to determine if they are native metals or oxides. For each spectrum, the area investigated is shown in the associated four images corresponding to different positions in the healed fracture. Crosses indicate locations in the large cluster and in the isolated inclusions where analyses were undertaken for the presence of metallic inclusions.*

### *3.6. X-ray diffraction of primary and secondary inclusions*

XRD analyses of both primary and secondary inclusions from three diamonds (B8-1, B16-1 and B20-1) revealed the presence of graphite in all inclusions and the coexistence of several phases, either trapped together or isolated (Table 3 and Supplementary Materials, figures A-F).

425 **Table 3.** Diffraction patterns of selected inclusions in type IIb diamonds from SXRD micro-
426 analysis. Synchrotron XRD patterns (wavelength 0.3738 Å) were processed with Rietveld
427 refinement. *bcc*-(Fe,Ni) alloy indicates a mixture mainly composed of Fe, while *fcc*-(Ni,Fe) alloy
428 is mainly composed of Ni.

| # | Mineral phase | Unit cell parameters Å |
|---|---|---|
| B20-1-3 | Graphite | a = 2.458, c = 6.443 |
| | *bcc*-(Fe,Ni) | a = 2.861 |
| | *fcc*-(Fe,Ni) | a = 3.572 |
| B20-1-6 | Graphite | a = 2.458, c = 6.419 |
| | Breyite | a = 6.619, b = 9.213, c = 6.552, α = 83.4, β = 75.99, γ = 69.88 |
| | *fcc*-(Ni,Fe) | a = 3.570 |
| B16-1-11 | NiO | a = 4.187 |
| B8-1-69 | Graphite | a = 2.464, c = 6.716 |
| | *bcc*-(Fe,Ni) | a = 2.868 |
| | *fcc*-(Ni,Fe) | a = 3.588 |

429

430 No $H_2O$ ice (VI or VII) could be identified, which is consistent with the amorphous character
431 of the hydrous phase either surrounding the graphite crystals in secondary inclusions (Figs. 5E and
432 5F) or forming the halo in primary inclusions (Fig. 5C).

433 In all investigated inclusions, Fe-Ni metallic phases are present, which is coherent with both
434 the XRF investigation of samples B6-1, B8-1, B16-1 and B20-1 (Supplementary Materials A-F)

and the EDX analyses of diamond B16-1 (Table 2). Furthermore, two different Fe-Ni alloys have been identified using XRD: one Fe-rich alloy (Ni < 0.3), which crystallized in the *bcc* group (hereafter referred to as "*bcc*-(Fe,Ni)") and a Ni-rich alloy, which crystallized in the *fcc* group (referred to as "*fcc*-(Ni,Fe)") (Table 3). If an ambient pressure is assumed, the *fcc*-(Ni,Fe) unit cell parameter would correspond to a composition of 0.5 < Ni < 0.6 (Cacciamani et al., 2010). However, it should be noted that since the unit-cell parameters are both pressure- and composition-dependent, it is not possible to determine the composition and remnant pressure from the XRD measurements alone. One inclusion exhibiting a rock-salt structure was identified in sample B16-1, with an XRD intensity peak consistent with NiO but likely with some substitutions with Fe or Mg, as indicated by both the unit-cell parameters and the SEM-EDX analyses. The XRD analyses of primary inclusions trapped in diamond B20-1 show that graphite and *fcc*-(Ni,Fe) are trapped together with a breyite inclusion. The cell parameters of the breyite indicate low residual pressures at ambient temperature.

### *3.7 Entrapment pressure calculation*

The Raman spectrum of an isolated primary inclusion of breyite in diamond B6-1 exhibits three shifted peaks at 663, 990 and 1050 $cm^{-1}$ compared to the expected values of 656, 977 and 1037 $cm^{-1}$ at ambient conditions (Fig. 8A). Based on calibration curves obtained at different pressures by Anzolini et al. (2018), our observed Raman shifts on the B6-1 isolated breyite would correspond to a remnant pressure of 2.5 GPa (Anzolini et al., 2018). In diamond B20-1, graphite and hydrous phases coexist with primary inclusions which were identified by XRD as breyite, *fcc*-(Ni,Fe) and *bcc*-(Fe,Ni), while no oxides were detected. Assuming the experimental equation of

456 state of Anzolini et al. (2016) and a unit cell volume of 363.78 Å, the residual pressure determined
457 from the XRD patterns for B20-1 breyite is 2.8 GPa.

458 It has been shown that the potential presence of undetected micro-cracks in the host diamond
459 surrounding breyite inclusions (even the smallest, with a diameter of < 12 μm) may induce a
460 pressure drop and an underestimation of the real diamond formation depth (Anzolini et al., 2016).
461 To the best of our knowledge, breyite inclusions in B6-1 and B20-1 diamonds do not display
462 decompression fractures of any sort. The similar residual pressures of 2.5 and 2.8 GPa calculated
463 from isolated breyites contained in two different diamonds, and using two different techniques
464 (micro-Raman spectroscopy and XRD), are evidence of the absence of decompression fractures,
465 as their presence would otherwise result in random residual pressures.

466 Based on the obtained remnant pressures from the Raman shifts and XRD measurements in
467 the two isolated primary inclusions of breyite from samples B6-1 and B20-1, it is possible to
468 calculate the minimal entrapment pressure of inclusions using elastic geothermobarometry (Angel
469 et al., 2014). Trapping pressures were calculated using the EosFit-Pinc software (Angel et al.,
470 2017). It is worth noting that both B6-1 and B20-1 diamonds contain other breyites, but, here, are
471 associated with larnites (e.g., Fig. 10B). In presence of multi-phased inclusions, trapping pressures
472 cannot be correctly calculated due to the risk of each of the mineral pairs reacting elastically in a
473 different way, resulting in an underestimation of the remnant pressures (e.g., Cisneros and Befus,
474 2020). By applying a pressure correction induced by elastic relaxation, as proposed by Angel et
475 al., (2017), a trapping pressure of 2.5 GPa at 900-1400 °C would result in a recalculated pressure
476 of the isolated breyites in samples B6-1 and B20-1 ranging from 4.9 to 5.6 GPa, indicative of a
477 formation depth between 160 to 180 km. Although these remain minimum estimated pressures,

their consistency is striking, and collectively point to a lithospheric origin for the studied diamonds.

## 4. Discussion

### *4.1 Where do type IIb diamonds form in the mantle?*

Consistent trapping pressure estimates from primary breyite inclusions in two different samples – as well as the mineralogy of their principal inclusions, such as larnite and graphite – suggest lithospheric formation depths between 160 to 180 km for our studied diamonds. Given that our proposed origin could be distinct with some of the available literature, hereafter, we provide a review of breyite and larnite stability and genesis.

Breyite and its high-pressure equivalent $CaSiO_3$-perovskite can be formed throughout the entire mantle and their presence alone in a diamond does not provide univocal evidence for a lower mantle origin (Moore and Helmstaedt 2019; Fedoraeva et al., 2019; Brenker et al. 2020). Indeed, breyite in diamonds may have multiple origins. Some breyite can occur in lower mantle diamonds as a direct back-transformation product at 10 GPa of $CaSiO_3$-perovskite. However, Fedoraeva et al. (2019) have shown that breyite can also result from reaction between carbonate and $SiO_2$ or a Si-rich fluid. The direct crystallization of both breyite and larnite (as observed in diamonds B6-1 and B20-1; Figs. 5A) can occur at pressures of $\leq$ 6 GPa and temperatures of 1300-1750 °C in a carbonate/Ca-rich environment (Fedoraeva et al., 2019). Temperatures required to reach the formation of breyite in Fedoraeva's experiments are slightly higher than those expected at the calculated lithospheric depths of our samples, but it is worth noting that our diamonds contain abundant aqueous fluids. Abundant available water would enable a sufficient decrease in

499 temperatures during the reaction, allowing for the formation of breyite and larnite in the
500 lithosphere, which would otherwise be impossible under normal temperature conditions.

501 Phase diagram interpretation indicates that the coexistence of breyite and larnite necessitates
502 a trapping pressure within the range 6-9 GPa at 900-1400 ˚C at the lithosphere/asthenosphere
503 boundary (Gasparik et al., 1994; Brenker et al., 2005 and 2007; Fedoraeva et al., 2019).
504 Additionally, Fedoraeva et al. (2019) suggested that infiltration of a $CaCO_3$- $CaSiCO_3$ melt into a
505 more reduced peridotitic mantle (see section 4.2) would result in a partial reduction of $CaCO_3$ and
506 precipitation of both diamond, breyite and larnite at depths ranging from 160 to 180 km. These are
507 both viable scenarios for the formation of breyite and larnite inclusions at lithospheric depths in
508 our studied diamonds. The strong association of Si-bearing inclusions and a water-rich fluid
509 composition (large quantity of graphite-water inclusions) is coherent with the scenario of direct
510 crystallization of both breyite and larnite at moderate pressures.

511 A sublithospheric origin of breyite or a $CaSiO_3$ precursor would require its association with
512 other inclusions such as ferropericlase, low-Ni enstatite (bridgmanite) or high pressure olivine
513 polymorphs (e.g., Smith et al., 2018; Brenker et al., 2020). One such example is the association of
514 ringwoodite with presumably secondary breyite observed in a sublithospheric type IIa diamond
515 from Juina (sample JUc29; Pearson et al., 2014). None of these typical sublithospheric mineral
516 phases were found in any of our diamonds, lending further evidence to a possible origin in the
517 lower mantle. Furthermore, if the type IIb diamonds studied here were formed under
518 sublithospheric trapping conditions, ice should be observed in inclusions at room temperature (e.g.
519 ice VII inclusions; Tschauner et al., 2018), whereas the XRD investigation did not reveal any
520 presence of any ice in the inclusions analyzed.

521 The lithospheric depths of diamond formation obtained from our recalculated residual
522 pressures are also consistent with the presence of primary graphite inclusions (those not related to
523 the healed fractures; Fig. 10A-D), which points to the crystallization of diamonds close to the
524 graphite-diamond inversion curve, corresponding to conditions of 4-4.5 GPa and 1200-1400 ˚C
525 (e.g., Bulanova, 1995; Day, 2012). Based on the observed mineralogy in our samples and previous
526 studies of Smith et al. (2018), we conclude that type IIb diamonds are capable, under certain
527 conditions, of growing within a mantle continuum, ranging from lithospheric to sublithospheric
528 depths.

529 *4.2 Type IIb diamond parental fluids*

530 This study documents that natural type IIb diamonds grow in the presence of fluids. This is
531 a well-accepted concept but the fluids can be diverse both chemically and from their redox state
532 (oxidized or reduced). In this section, different models for diamond formation are reviewed in
533 order to propose a credible scenario for lithospheric-grown type IIb diamonds.

534 Synthetic diamond growth typically occurs through carbon supersaturation of metallic alloys
535 (e.g. Bataleva et al., 2016) and type IIb diamonds can be synthesized at lithospheric conditions,
536 under reduced conditions. Chepurov et al. (2007) grew type IIb diamonds from a mixture of
537 graphite as the carbon source, FeNi and FeCo alloys as solvents and $B_2O_3$ as the boron source.
538 Even if this mechanism contrasts with natural diamond formation complex redox reactions (e.g.
539 Pal'Yanov et al., 2005, 2013), these synthetic diamonds show some similarities with our natural
540 samples, in particular with respect to the occurrence of metallic inclusions.

541 The coexistence of reduced and oxidized species in diamonds suggests redox reactions: for
542 example, Fe-C melt in equilibrium with FeO could dissolve up to 0.5 wt.% O (Sokol et al., 2017).
543 As it subsequently cools and crystallizes, oxygen would be released, yielding oxidized species.

544 Here, inclusions of primary Fe-Ni-Cu alloys, FeNi and FeNiO (Table 3), attest to the
545 presence of metallic phases at lithospheric depths. This suggests that $fO_2$ should be sufficiently
546 low to stabilize Fe-alloys even at lithospheric pressures, where $fO_2$ is generally considered to be
547 above the iron-wüstite (IW) buffer. This assemblage is rare but not unusual. Stachel et al. (1998)
548 reported the presence of Fe, FeS, FeNiS and FeO inclusions and a solid solution of Fe-FeO-$Fe_3O_4$
549 as inclusion in lithospheric diamonds from the Mwadui Mine, Tanzania. They also reported an
550 inclusion consisting of a core of native iron rimmed by wüstite. Such an association might be
551 interpreted as evidence of redox processes, possibly associated with oxidized fluids. Indeed, the
552 presence of native iron, wüstite and magnetite in the same diamond indicated a variation in oxygen
553 fugacities from below iron-wüstite (IW) to above the wüstite-magnetite (WM) buffer. Stachel et
554 al. (1998) proposed diamond formation over a large range of $fO_2$ conditions, possibly along redox
555 fronts. These conditions recall those of high-pressure (6 GPa) diamond synthesis from Mg-Ca-
556 carbonates and metallic Fe at dry conditions (Pal'yanov et al., 2013). Diamonds would form both
557 ahead of and behind the redox front because of the presence of a $fO_2$ gradient. However, the above-
558 cited studies do not consider the presence of water, as observed in the primary and secondary
559 inclusions of the natural type IIb diamond studied here.

560 The presence of breyite and larnite in our diamonds could result from the reduction of Ca-
561 rich silico-carbonatitic fluids enriched in solutes (Fedoraeva et al., 2019), consistent with the
562 inclusions mineral assemblage from diamond B16-1 (Table 2; Fig. 7E). Some experimental studies

563 have demonstrated the significant role played by carbonate-bearing hydrous fluids in the growth
564 of diamonds (e.g., Pal'yanov et al., 1999; Sokol and Pal'yanov, 2008; Bureau et al., 2016; 2018)
565 and as a vector for determining the diamond's carbon source (e.g. Weiss et al., 2014; Jablon and
566 Navon, 2016 for natural samples).

567 In the type IIb diamonds analyzed in this study, diamond and graphite are in equilibrium
568 together with abundant water. Both graphite and $CH_4$-syngenetic inclusions were reported in
569 mixed-habit Type Ia (i.e., N-bearing) diamonds from Marange in Zimbabwe (Smit et al., 2016). In
570 the latter case, the intimate association of $CH_4$ and graphite suggests that both phases co-
571 crystallized from the diamond parent fluid. In the diamond stability field, it has also been proposed
572 that as hydrocarbon concentration in the aqueous fluid increases, initial diamond crystallization
573 gives way to co-crystallization of both diamond and graphite, followed ultimately by
574 crystallization of only graphite (Sokol et al., 2009).

575 In type IIb diamonds – and in Marange diamonds (Smit et al., 2016) – graphite would
576 crystallize before diamond and would subsequently be trapped or serve as the seed for further
577 diamond formation (Bulanova, 1995) during the fast diamond growth phase facilitated by the
578 presence of water (Bureau et al., 2016). In this model, it is expected that diamonds should contain
579 an abundance of nitrogen, as in the case of the Marange Mine diamonds. Here, the absence of
580 nitrogen could be explained by the presence of metal and sulfur that would prevent the nitrogen
581 from being incorporated into the diamonds (see next section).

582 Stachel et al. (2017) suggested that diamond formation in peridotite would not occur with
583 rock-buffered reactions, but rather would be buffered by the fluid itself, following the oxygen
584 conservative reaction in the lithosphere (Deines, 1980):

585 $$CO_2 + CH_4 = 2C + 2H_2O \quad (1)$$

586 and assuming that all available $CO_2$ (or carbonate solutes dissolved in a hydrous/silicic fluid or
587 methane) is consumed during diamond and/or graphite crystallization. However, in this model,
588 diamond growth is supposed to occur at the water maximum (i.e., for a fluid consisting almost
589 exclusively of $H_2O$ with minor $CH_4$ and $CO_2$; Foley, 2011; Stachel et al., 2017) at near constant
590 and buffered $fO_2$ close to FMQ-1, -2 (Fayalite-Magnetite-Quartz), corresponding to the conditions
591 of the redox EMOD reaction (Stachel et al., 2017). This model contrasts with the presence of
592 metallic liquids mingled with the aqueous fluid. Type IIb diamond formation may be closer to the
593 model for crystallization of Fe alloys, in association with diamonds that reacted with a surrounding
594 silicate proposed by Jacob et al. (2004). Citing a polycrystalline diamond of inferred lithospheric
595 provenance exhibiting cohenite, native iron and troilite enclosed within a garnet inclusion, they
596 suggest that the inclusions in the garnets reflect local and probably transient conditions within the
597 lithosphere, linked to diamond formation within a C-O-H fluid that reacted with the surrounding
598 silicate.

599 One could argue that the source of carbon for diamond growth may be a metallic liquid
600 (e.g., Smith et al., 2016), as experimentally achieved from mixture of FeNiS metals and iron
601 carbides at mantle conditions (Bataleva et al., 2016). In the absence of iron carbides, carbon may
602 be dissolved in these metallic melts, as demonstrated, for example, by experimental pressures of
603 1-15 GPa and temperatures of 1600-2300 °C inducing the solubility of carbon in FeNi metallic
604 liquids in equilibrium with silicates reaching a few wt.% (e.g., Malavergne et al., 2019). It is worth
605 noting that formation of our studied type IIb diamonds in a metal melt, a possible formation
606 mechanism proposed by Smith et al. (2014; 2016), it is however highly unlikely here. Our data

illustrate that the mantle environment where these type IIb diamonds grew is particularly rich in water. With even the slightest presence of water in the melt (>0.5 % of water), diamond growth will be completely inhibited, with graphite forming instead of diamond (Pal'yanov et al., 2012).

Type IIb diamond formation may be described by the following simplified equation:

$$[3CaCO_3 + 2SiO_2]melt + 2H_2O + 9FeNi = FeNi + 8FeNiO + CH_4 + CaSiO_3 + Ca_2SiO_4 + 2C \quad (2)$$

In this scenario, the carbon source may be multiple: $CO_3^{2-}$ or $CO_2$ dissolved in a melt and possibly trace amount of C initially dissolved and released during crystallization of FeNi and FeNiO.

Based on the presence of Ca-bearing silicate minerals and C-O-H fluids in the studied diamonds, the above scenario, involving carbonate reduction causing the formation of larnite and breyite, but also possibly hydrous ferrous sulfate exhibiting a pre-existing ferricopiatite-like structure in the host-rock. Combination reactions for carbonate reduction would release methane, metal alloys and metal oxides, and silicate minerals, such as breyite and larnite, trapped in type IIb diamonds during their syngenetic growth. In this model, N would be sequestrated/scavenged by the metallic phase (Sokol et al., 2019) and/or by sulfur. Type IIb diamonds growing in fluids introduced in highly reduced conditions would thus not incorporate any nitrogen. In this model the graphite-$CH_4$ assemblage would represent the residual rather than the primitive fluid.

*4.3. B- and N- poor type IIb diamonds: the key to identifying their growth environment*

Nitrogen content in diamonds, including their core-to-rim variations, is commonly interpreted as relating to their host fluid through their melt/fluid-diamond partitioning coefficient

628 (Deines et al., 1989; Cartigny et al., 2001; Stachel et al., 2009), with this interpretation having been
629 used in previous studies (e.g. Thomassot et al., 2007; Smit et al., 2016).

630 The occurrence of boron in type IIb diamonds has led to the widespread adoption of the
631 term "boron-rich diamond". Linking type IIb diamond genesis with fluids derived from "B-rich
632 environments", in particular subducted serpentinites (e.g., Smith et al., 2018a), however, suffers
633 from several shortcomings. Notably, B-recycling in the mantle, at depths beyond those of the back-
634 arc (100 km), is the object of ongoing debate (De Hoog and Savov, 2018), with some researchers
635 suggesting recently that boron is actually not subducted in the deep mantle at all (McCaig et al.,
636 2018). Furthermore, with a maximum B value of 10 atomic ppm, the B/C-ratios of type IIb
637 diamonds are low, $< 10 \times 10^{-6}$, with this value remaining approximately three orders of magnitude
638 lower than that of the depleted or primitive mantle (B/C-ratio of approximately $6800 \times 10^{-6}$,
639 computed from ~0.3 ppm B and ~49 ppm C; McDonough and Sun, 1995; Chaussidon and Jambon,
640 1994; Cartigny et al., 2008; Le Voyer et al., 2017). Thus, the need to relate type IIb diamonds are
641 related to B-rich subducted serpentinites appears unjustified given that Earth's mantle is
642 sufficiently rich in boron at ~ 8 ppm to account for the B-content of type IIb diamonds (Gaillou et
643 al., 2012).

644 In our view, the fundamental observation informing the origin of type IIb diamonds is not
645 related to the occurrence of "high" boron content in these diamonds, but rather their low B-content
646 coupled with even lower levels of nitrogen. Given that both the convective mantle and subducted
647 material contain substantial amounts of nitrogen (e.g. Cartigny and Marty, 2013 for a review of
648 mantle nitrogen; Philippot et al., 2007; Cannaò et al., 2020 for a review of subducted serpentinites),
649 ensuring the presence of nitrogen in both the mantle and subducted serpentinite derived

650 fluids/melts, boron, if present, would be prevented from expressing the typical spectroscopic
651 features found in type IIb diamonds.

652 Nitrogen partitioning (Kd-values) between fluid and diamond has been deduced or
653 suggested in a number of previous studies, though the extent to which the phenomenon is said to
654 occur varies substantially and no consensus has yet been reached (e.g., Cartigny et al., 2014 for a
655 review on the subject). In the case of $CH_4$-rich fluids, two phenomena would be expected to occur:
656 given the compatible behavior of N (Thomassot et al., 2007; Stachel et al., 2017), the fluid would
657 become increasingly N-depleted with the progression of diamond crystallization while
658 simultaneously becoming $^{13}C$-depleted owing to the partitioning of C-isotopes between diamond
659 and $CH_4$ (Cartigny et al., 2014). These diamonds would therefore have low $\delta^{13}C$-values, as can be
660 inferred from the few available data for large type II diamonds (from -20.8 to -1.8‰ vs. V-PDB;
661 Milledge et al., 1983; Smith et al., 2018a) in addition to having low N-contents, making the
662 presence of boron in these diamonds possible only when the partitioning value of boron in the fluid
663 is less than that of nitrogen. To the best of our knowledge, no Kd-values between fluid and
664 diamond have been determined for boron, leaving open the possibility that type IIb diamonds
665 indeed grow from fluids with high B/C-ratios, albeit with very low Kd-values (i.e., boron would
666 be incompatible with respect to diamond). Given that significant amounts of boron (> 1000 at.ppm)
667 can be incorporated into synthetic diamonds (Polyakov et al., 2001), the low B-content of type IIb
668 diamonds might reflect low B/C-ratios of the parental fluid at elevated Kd-values (ie., > 1). Still,
669 a preferable explanation is that the low N-character reflects low oxygen fugacities. Under metal-
670 saturation conditions, nitrogen would be sequestrated in the metal phase (Sokol et al., 2019),
671 whether the fluid derives from a reduced environment or, as documented here, from crystallization

672 of the diamond in oxidized fluids introduced in a reduced environment. Bolstering this argument,
673 experimental studies have suggested that in the metal-fluid system, nitrogen has a higher affinity
674 for iron and selectively accumulates in the metal phase, while some mobile carbon resides in the
675 fluid phase (Sokol et al., 2018).

676 The sequestration of N in metals can explain the absence of nitrogen in large
677 sublithospheric type II diamonds carrying metallic inclusions (Smith and Kopylova, 2014; Smith
678 et al, 2016). Given that boron is a lithophile element, the fluids/melts would, in a reduced
679 environment, develop rather high B/N-ratios. In this case, B-poor, nitrogen-free type IIb diamonds
680 would characterize the most reduced environment for diamond formation. An alternative
681 hypothesis for explaining the absence of N could be related to its speciation in the mantle as $N_2$ or
682 $NH_4^+$, both of which are incompatible in the diamond lattice into which nitrogen substitutes for
683 carbon as single atoms (Mikhail and Howell, 2016).

684 **5. Conclusions**

685 A detailed study of type IIb diamonds from the Cullinan Mine, South Africa, allowed
686 identification of hydrous fluids in primary and secondary inclusions, associated with methane,
687 graphite, metallic alloys, sulfides and oxides. The most important conclusions of this study are:

688 1) The mineralogical assemblage of primary inclusions shows the presence of breyite ± larnite
689 and graphite. Breyite inclusions were used to estimate residual pressures of 2.5-2.8 GPa
690 corresponding to minimal entrapment pressures of 4.9 to 5.6 GPa at the typical temperature
691 range of 900-1400˚C, otherwise known as the “diamond window”. These physical
692 conditions – together with the presence of breyite ± larnite and graphite inclusions and the

absence of typical sublitospheric mineral association of $CaSiO_3$ + ferropericlase, low-Ni enstatite or olivine polymorphs – are more consistent with lithospheric depths of formation for type IIb diamonds, which were, until now, considered only of sublitospheric origin (Smith et al., 2018a and b).

2) The type IIb diamonds studied here revealed numerous mineral and fluid inclusions: a hydrous phase ($H_2O$, OH) with $CH_4$ and solute, Fe-Ni oxides, hydrous ferrous sulfates and Fe-Ni±Cu alloys. The coexistence of reduced and oxidized species suggests complex redox reactions, where the $fO_2$ should be sufficiently low for Fe-alloys to be stable under lithospheric pressures; it may reflect local and probably transient conditions within the lithosphere (Jacob et al., 2004), linked to the equilibrium of diamond with C-O-H fluids such as those identified in the studied type IIb diamonds.

3) Finally, the lack of nitrogen and the presence of only negligible boron in type IIb diamonds does not ultimately require a link with subduction setting, given Earth's mantle is sufficiently B-rich to account for the formation of type IIb diamonds, while simultaneously nitrogen is likely sufficiently sequestered by metallic alloys accompanying growth fluids to explain its absence.

It is not the intent of the authors here to refute the sublithospheric origin of type IIb blue diamonds proposed by Smith et al. (2018a, b) and based on mineral assemblages typical of the lower mantle. Rather, we seek to suggest, based on our results suggesting lithospheric depths of formation, that type IIb diamonds form in a mantle continuum, from sublithospheric to lithospheric depths. In proposing this new framework for type IIb diamond formation and discussing the conditions under which it is viable, this work highlights the limited knowledge available

concerning these peculiar diamonds, stemming principally from the absence of sufficient samples to study. The mineral and fluid inclusion assemblages observed here, together with previous results from Smith et al. (2018a,b), will be crucial in developing a well-constrained model of the formation of type IIb diamonds.

**Acknowledgements**

This manuscript benefited from informal reviews from Ingrid Chinn and Thomas Stachel of earlier versions of the manuscript. The handling editor S. Aulbach, Alex Sokol and an anonymous reviewer are thanked for their constructive and thoughtful criticisms. We greatly acknowledge De Beers Consolidated Mines for the donation of the diamonds, including Ingrid Chinn for her support. This project is funded by Sorbonne Université EMERGENCE program (HYDRODIAMS to HB), TelluS Program of the CNRS-INSU, GEOTOP and FRQNT for an international internship to LD, and NSERC Discovery grant RGPIN-2015-05378 for funding LD doctoral fellowship. The SEM facility of IMPMC is supported by Région Ile de France Grant SESAME 2006 NOI-07-593/R, INSU-CNRS, INP-CNRS, UPMC, and by the French National Research Agency (ANR) Grant ANR-07-BLAN-0124-01. The authors wish to acknowledge the French Gem Lab LFG (Laboratoire Français de Gemmologie) for confirming some of the FTIR results, especially Annabelle Herreweghe and Stefanos Karampelas. We thank M. Guillaumet from the IMPMC spectroscopy platform, Ludovic Delbes, Philippe Rosier from the IMPMC cellule project, and Christophe Sandt and Ferenc Borondics from the SMIS beamline at SOLEIL synchrotron for their support during micro-Raman spectral imaging. We thank Ross Angel for his kind help and advice on the calculation of pressure correction for elastic relaxation.

## References


Allsopp, H.L., Bristow, J.W., Smith, C.B., Brown, R., Gleadow, A.J.W., Kramers, J.D., Garvie, O.G., 1989. A summary of radiometric dating methods applicable to kimberlites and related rocks. Geological Society Australia Special Publication 14, 343–357.

Angel, R.J., Mazzucchelli, M.L., Alvaro, M., Nimis, P., Nestola, F., 2014. Geobarometry from host-inclusion systems: the role of elastic relaxation. American Mineralogist 99, 2146-2149.

Angel, R.J., Mazzucchelli, M.L., Alvaro, M., Nestola, F., 2017 EosFit-Pic: a simple GUI for host-inclusion elastic thermobarometry. American Mineralogist 102, 1957-1960.

Anthony, J.W., Bideaux, R.A., Bladh, K.W. and Nichols, M.C., 2000. Handbook of Mineralogy, Volume 4, Arsenates, Phosphates, Vanadates: Tucson, Arizona, Mineral Data Publishing.

Anzolini, C., Angel, R.J., Merlini, M., Derzsi, M., Tokár, K., Milani, S., Harris, J.W., 2016. Depth of formation of $CaSiO_3$-walstromite included in super-deep diamonds. Lithos 265, 138-147.

Anzolini, C., Prencipe, M., Alvaro, M., Romano, C., Vona, A., Lorenzon, S., Nestola, F., 2018. Depth of formation of super-deep diamonds: Raman barometry of $CaSiO_3$-walstromite inclusions. American Mineralogist 103, 69-74.

Auer, B.M., Skinner, J.L., 2008. IR and Raman spectra of liquid water: Theory and interpretation. Journal of Chemical Physics 128, 224511.

Bataleva, Y.V., Palyanov, Y.N., Borzdov, Y.M., Sobolev, N.V. 2016. Graphite and diamond formation via the interaction of iron carbide and Fe,Ni-sulfide under mantle P–T parameters. Doklady Earth Sciences 471,1144-1148.

757 Brenker, F.E., Vincze, L., Vekemans, B., Nasdala, L., Stachel, T., Vollmer, C., Kersten, M.,
758 Somogyi, A., Adams, F., Joswig, W., Harris, J.W., 2005. Detection of Ca-rich lithology in
759 the Earth's deep (> 300) convecting mantle. Earth and Planetary Science Letters 236, 579-
760 587.

761 Brenker, F.E., Nestola, F., Brenker, L., Peruzzo, L., Harris, J.W., 2020. Origin, properties and
762 structure of breyite: the second most abundant mineral inclusion in super-deep diamonds.
763 American Mineralogist 106, 38-43.

764 Bulanova, G.P., 1995. The formation of diamond. Journal of Geochemical Exploration 53, 1-23.

765 Bureau, H., Frost, D.J., Bolfan-Casanova, N., Leroy, C., Esteve, I., Cordier, P., 2016. Diamond
766 growth in mantle fluids, Lithos 265, 4-15.

767 Bureau, H., Remusat, L., Esteve, I., Pinti, D.L., Cartigny, P., 2018. The growth of lithospheric
768 diamonds. Science Advanced 4, 1602-1607.

769 Cacciamani, G., Dinsdale, A., Palumbo, M., Pasturel, A., 2010. The Fe–Ni system: thermodynamic
770 modelling assisted by atomistic calculations. Intermetallics 18, 1148-1162.

771 Cannaò, E., Tiepolo, M., Bebout, G.E., Scambelluri, M., 2020. Into the deep and beyond: Carbon
772 and nitrogen subduction recycling in secondary peridotites. Earth and Planetary Science
773 Letters 543, 116328.

774 Cartigny, P., Harris, J.W., Javoy, M . 2001. Diamond genesis, mantle fractionations and mantle
775 nitrogen content: a study of $\delta^{13}$C-N concentrations in diamonds. Earth and Planetary
776 Sciences Letters 185, 85-98.

777 Cartigny, P., Pineau, F., Aubaud, C., Javoy, M., 2008. Towards a consistent mantle carbon flux
778 estimate: Insights from volatile systematics ($H_2O$/Ce, δD, $CO_2$/Nb) in the North Atlantic
779 mantle (14° N and 34° N). Earth and Planetary Science Letters 265, 672-685.

780 Cartigny, P., Marty, B., 2013. Nitrogen isotopes and mantle geodynamics: The emergence of life
781 and the atmosphere–crust–mantle connection. Elements 9, 359-366.

782 Cartigny, P., Palot, M., Thomassot, E., Harris, J.W., 2014. Diamond formation: a stable isotope
783 perspective. Annual Review of Earth and Planetary Sciences 42, 699-732.

784 Chaussidon, M., Jambon, A., 1994. Boron content and isotopic composition of oceanic basalts:
785 geochemical and cosmochemical implications. Earth and Planetary Science Letters 121,
786 277-291.

787 Chepurov, A.I., Zhimulev, E.I., Fedorov, I.I., Sonin, V.M., 2007. Inclusions of metal solvent and
788 color of boron-bearing monocrystals of synthetic diamond. Geology of Ore Deposits 49,
789 648-651.

790 Chrenko, R.M., 1973. Boron, the dominant acceptor in semiconducting diamond. Physical Review
791 B 7, 4560-4567.

792 Cisneros, M., Befus, K. S. (2020). Applications and limitations of elastic thermobarometry:
793 Insights from elastic modeling of inclusion-host pairs and example case studies.
794 Geochemistry, Geophysics, Geosystems, 21, e2020GC009231.

795 Collins A.T., 1982. Colour centres in diamond. Journal of Gemmology, Vol. 18, No. 1, pp. 37-75.

796 Day, H. W., 2012. A revised diamond-graphite transition curve. American Mineralogist, 97(1),
797 52-62.

798 De Hoog, J.C.M., Savov, I.P., 2018. Boron isotopes as a tracer of subduction zone processes, in:
799 Marschall, H., Foster, G. (Eds.), Boron Isotopes: The Fifth Element, pp. 217-247.

800 Deines, P., 1980. The carbon isotopic composition of diamonds: relationship to diamond shape,
801 color, occurrence and vapor composition. Geochimica et Cosmochimica Acta 44, 943-961.

802 Deines, P., Harris, J.W., Spear, P.M., Gurney, J.J., 1989. Nitrogen and $^{13}C$ content of Finsch and
803 Premier diamonds and their implications. Geochimica et Cosmochimica Acta 53, 1367-
804 1378.

805 Downs, R.T., Hall-Wallace, M., 2003. The American Mineralogist crystal structure database.
806 American Mineralogist 88, 247-250.

807 Fedoraeva, A.S., Shatskiy, A., Litasov, K.D., 2019. The join $CaCO_3$-$CaSiO_3$ at 6 GPa with
808 implication to Ca-rich lithologies trapped by kimberliteic diamonds. High Pressure
809 Research, 39, 547-560.

810 Ferrari, A.C., 2007. Raman spectroscopy of graphene and graphite: Disorder, electron–phonon
811 coupling, doping and nonadiabatic effects. Solid State Communications 143, 47-57.

812 Fisher, D., Sibley, S.J., Kelly, C.J., 2009. Brown colour in natural diamond and interaction
813 between the brown related and other colour-inducing defects. Journal of Physics: Condensed
814 Matter, 21, 1-10.

Frost, D.J., McCammon, C.A., 2008. The redox state of Earth's mantle. Annual Review of Earth and Planetary Sciences 36, 389-420.

Foley, S. F., 2011. A Reappraisal of Redox Melting in the Earth's Mantle as a Function of Tectonic Setting and Time, Journal of Petrology, Volume 52, Issue 7-8, Pages 1363–1391.

Gaillou, E., Post, J.E., Rost, D., Butler, J.E., 2012. Boron in natural type IIb blue diamonds: Chemical and spectroscopic measurements. American Mineralogist 97, 1-18.

Gasparik, T., Wolf, K., Smith, C.M., 1994. Experimental determination of phase relations in the $CaSiO_3$ system from 8 to 13 GPa. American Mineralogist 79, 1219-1222.

Glinnemann, J., Kusaka, K., Harris, J.W., 2003. Oriented graphite single-crystal inclusions in diamond. Zeitschrift für Kristallographie-Crystalline Materials 218, 733-739.

Harte, B., 2010. Diamond formation in the deep mantle: the record of mineral inclusions and their distribution in relation to mantle dehydration zones. Mineralogical Magazine 74, 189–215.

Jablon, B.M., Navon, O. 2016. Most diamonds were created equal. Earth and Planetary Sciences Letters 443, 41-47.

Jacob, D.E., Kronz, A., Viljoen, K.S., 2004. Coehnite, native iron and troilite inclusions in garnets from polycrystalline diamond aggregates. Contribution to Mineralogy and Petrology, 146, 566-576.

Joswig, W., Stachel, T., Harris, J. W., Baur, W. H., Brey, G. P., 1999. New Ca-silicate inclusions in diamonds—tracers from the lower mantle. Earth and Planetary Science Letters, 173(1-2), 1-6.

King, J.M., Moses, T.M., Shigley, J.E., Welbourn, C.M., Lawson, S.C., Cooper, M., 1998. Characterizing natural-color type IIb blue diamonds. Gems & Gemology 34, 246-268.

Le Voyer, M., Kelley, K.A., Cottrell, E., Hauri, E.H., 2017. Heterogeneity in mantle carbon content from $CO_2$-undersaturated basalts. Nature Communications 8, 14062.

Malavergne, V., Bureau, H., Raepsaet, C., Gaillard, F., Poncet, M., Surblé, S., Sifré, D., Shcheka, S., Fourdrin, C., Deldicque, D., Khodja, H., 2019. Experimental constraints on the fate of H and C during planetary core-mantle differentiation. Implications for the Earth. Icarus 321, 473-485.

McCaig, A.M., Titarenko, S.S., Savov, I.P., Cliff, R.A., Banks, D., Boyce, A., Agostini, S., 2018. No significant boron in the hydrated mantle of most subducting slabs. Nature Communications 9, 4602.

McDonough, W.F., Sun, S.-S., 1995. The composition of the Earth. Chemical Geology 120, 223-253.

Men, Z., Fang, W., Li, D., Li, Z., Sun, C., 2014. Raman spectra from symmetric hydrogen bonds in water by high-intensity laser-induced breakdown. Scientific Reports 4, 4606.

Meyer H O A 1987 Mantle Xenoliths ed P H Nixon (Chichester: Wiley) pp 501–22

Mikhail, S., Howell, D., 2016. A petrological assessment of diamond as a recorder of the mantle nitrogen cycle. American Mineralogist, 101, 780-787.

Milledge, H.J., Mendelssohn, M.J., Seal, M., Rouse, J.E., Swart, P.K., Pillinger, C.T., 1983. Carbon isotopic variation in spectral type II diamonds. Nature 303, 791-792.

855 Moore, A. E., Helmstaedt, H., 2019. Evidence for two blue (type IIb) diamond populations. Nature
856 570, E26-E27.

857 Moser, D.E., Flowers, R.M., Hart, R.J., 2001. Birth of the Kaapvaal tectosphere 3.08 billion years
858 ago. Science 291, 465-469.

859 Nestola, F., Korolev, N., Kopylova, M., Rotiroti, N., Pearson, D.G., Pamato, M.G., Alvaro, M.,
860 Peruzzo, L., Gurney, J.J., Moore, A.E., Davidson, J., 2018. $CaSiO_3$ perovskite in diamond
861 indicates the recycling of oceanic crust into the lower mantle. Nature 555, 237-241.

862 Pal'yanov Y.N., Sokol A.G., Bozdov Y.M., Khokhryakov A.F., Sobolev N.V., 1999. Diamond
863 formation from mantle carbonate fluids. Nature 400, 417–418.

864 Pal'yanov, Y.N., Sokol, A.G., Tomilenko, A.A., Sobolev, N.V., 2005. Conditions of diamond
865 formation through carbonate-silicate interaction. European Journal of Mineralogy 17, 207–
866 214

867 Palyanov, Y. N., Borzdov, Y. M., Kupriyanov, I. N., Khokhryakov, A. F., 2012. Effect of H2O on
868 diamond crystal growth in metal–carbon systems. Crystal growth & design, 12(11), 5571-
869 5578.

870 Pal'yanov, Y.N., Bataleva, Y.V., Sokol, A.G., Borzdov, YM., Kupriyanov, I.N., Reutsky, V.N.,
871 Sobolev, N.V., 2013. Mantle–slab interaction and redox mechanism of diamond
872 formation. Proceedings of the National Academy of Sciences 110, 20408-20413.

873 Pearson, D. G., Brenker, F. E., Nestola, F., McNeill, J., Nasdala, L., Hutchison, M. T., Matveev,
874 S., Mather, K., Silversmit, G., Schmitz, S., Vekemans, B., Vincze, L., 2014. Hydrous mantle

transition zone indicated by ringwoodite included within diamond. Nature, 507(7491), 221-224.

Philippot, P., Busigny, V., Scambelluri, M., Cartigny, P., 2007. Oxygen and nitrogen isotopes as tracers of fluid activities in serpentinites and metasediments during subduction. Mineralogy and Petrology 91, 11-24.

Polyakov, V.I., Rukovishnikov, A.I., Rossukanyi, N.M., Ralchenko, V.G., 2001. Electrical properties of thick boron and nitrogen contained CVD diamond films. Diamond and Related Materials 10, 593-600.

Prescher, C., Prakapenka, V.B., 2015. DIOPTAS: a program for reduction of two-dimensional X-ray diffraction data and data exploration. High Pressure Research 35, 223–230.

Reich, S., Thomsen, C., 2004. Raman spectroscopy of graphite. Philosophical Transactions of the Royal Society of London. Series A: Mathematical, Physical and Engineering Sciences 362, 2271-2288.

Roedder, E., 1979. Origin and significance of magmatic inclusions. Bull. Mineral. 102, 487-510.

Schmitz, M.D., Bowring, S.A., de Wit, M.J., Gartz, V., 2004. Subduction and terrane collision stabilize the western Kaapvaal craton tectosphere 2.9 billion years ago. Earth and Planetary Science Letters 222, 363-376.

Schrauder, M., Navon, O., 1994. Hydrous and carbonatitic mantle fluids in fibrous diamonds from Jwaneng, Botswana. Geochimica et Cosmochimica Acta, 58(2), 761-771.

894 Scoates, J.S., Friedman, R.M., 2008. Precise age of the platiniferous Merensky Reef, Bushveld
895 Complex, South Africa, by the U–Pb zircon chemical abrasion ID-TIMS technique.
896 Economic Geology 103, 465–471.

897 Shatsky, V. S., Ragozin, A. L., Logvinova, A. M., Wirth, R., Kalinina, V. V., Sobolev, N. V.,
898 2020. Diamond-rich placer deposits from iron-saturated mantle beneath the northeastern
899 margin of the Siberian Craton. Lithos, 364, 105514.

900 Shirey, S. B., Cartigny, P., Frost, D. J., Keshav, S., Nestola, F., Nimis, P., Pearson, G., Sobolev,
901 N. V., Walter, M. J., 2013. Diamonds and the geology of mantle carbon. Reviews in
902 Mineralogy and Geochemistry, 75(1), 355-421.

903 Shirey, S.B., Smit, K., Pearson, G., Walter, M. J., Aulbach, S., Brenker, F. E., Bureau, H.,
904 Burnham, A. D., Cartigny, P., Chacko, T., Frost, D. J., Hauri, E. J., Jacob, D. E., Jacobsen,
905 S. D., Kohn, S. C., Luth, R. W., Mikhail, S., Navon, O., Nestola, F., Nimis, P., Palot, M.,
906 Smith, E. M., Stachel, T., Stagno, V., Steele, A., Stern, R. A., Thomassot, E., Thomson, A.
907 R., Weiss, Y., , 2019. Diamonds and the mantle geodynamics of carbon: deep mantle carbon
908 evolution from the diamond record, in: Orcutt, B., Daniel, I. Dasgupta, R. (Eds.), Deep
909 Carbon: Past to Present . Cambridge University Press, Cambridge, pp. 89-128.

910 Smit, K.V., Shirey, S.B., Stern, R.A., Steele, A., Wang, W., 2016. Diamond growth from C–H–
911 N–O recycled fluids in the lithosphere: Evidence from $CH_4$ micro-inclusions and $\delta^{13}C$–$\delta^{15}N$–
912 N content in Marange mixed-habit diamonds. Lithos 265, 68-81.

913 Smith, E.M., Kopylova, M., 2014. Implications of metallic iron for diamonds and nitrogen in the
914 sublithospheric mantle. Canadian Journal of Earth Sciences 51, 510-516.

915 Smith, E.M., Shirey, S.B., Nestola, F., Bullock, E.S., Wang, J., Richardson, S.H., Wang, W., 2016.
916 Large gem diamonds from metallic liquid in Earth's deep mantle. Science 354, 1403-1405.

917 Smith, E.M., Shirey, S.B., Richardson, S.H., Nestola, F., Bullock, E.S., Wang, J., Wang, W.,
918 2018a. Blue boron-bearing diamonds from Earth's lower mantle. Nature, 560, 84-87.

919 Smith, E.M., Shirey, S.B., Richardson, S.H., Nestola, F., Bullock, E.S., Wang, J., Wang, W.,
920 2018b. Reply to: Evidence for two blue (type IIb) diamond populations. Nature 570,
921 doi.org/10.1038/s41586-019-1246-8.

922 Smith, E. M., Ni, P., Shirey, S. B., Richardson, S. H., Wang, W., Shahar, A., 2021. Heavy iron in
923 large gem diamonds traces deep subduction of serpentinized ocean floor. Science
924 Advances, 7(14), eabe9773.

925 Sokol, A.G., Pal'yanov, Y.N., 2008. Diamond formation in the system MgO–$SiO_2$–$H_2O$–C at 7.5
926 GPa and 1600 °C. Contribution to Mineralogy and Petrology 155, 33–43.

927 Sokol, A. G., Palyanova, G. A., Palyanov, Y. N., Tomilenko, A. A., & Melenevsky, V. N., 2009.
928 Fluid regime and diamond formation in the reduced mantle: Experimental
929 constraints. Geochimica et Cosmochimica Acta, 73(19), 5820-5834.

930 Sokol, A. G., Kruk, A. N., Seryotkin, Y. V., Korablin, A. A., & Palyanov, Y. N., 2017. Phase
931 relations in the Fe-Fe3C-Fe3N system at 7.8 GPa and 1350° C: Implications for carbon and
932 nitrogen hosts in Fe0-saturated upper mantle. Physics of the Earth and Planetary Interiors,
933 265, 43-53.

934 Sokol, A. G., Tomilenko, A. A., Bul'bak, T. A., Kruk, A. N., Zaikin, P. A., Sokol, I. A., Seryotkin,
935 Y. V., Palyanov, Y. N. (2018). The Fe–C–O–H–N system at 6.3–7.8 GPa and 1200–1400°

C: implications for deep carbon and nitrogen cycles. Contributions to Mineralogy and Petrology, 173(6), 1-17.

Sokol, A.G., Khokhryakov, A.F., Borzdov, Y.., Kupriyanov, I.N., Palyanov, Y.N., 2019. Solubility of carbon and nitrogen in a sulfur-bearing iron melt: Constraints for siderophile behavior at upper mantle conditions. American Mineralogist104, 1857-1865.

Stachel, T., Harris, J.W., Brey, G.P., 1998. Rare and unusual mineral inclusions in diamonds from Mwadui, Tanzania. Contribution to Mineralogy and Petrology 132, 34-47.

Stachel, T., Harris, J.W., Muehlenbachs, K. 2009. Sources of carbon in inclusions bearing diamonds. Lithos 112, 625-637.

Stachel, T., Chacko, T., Luth, R.W., 2017. Carbon isotope fractionation during diamond growth in depleted peridotite: Counterintuitive insights from modelling water-maximum CHO fluids as multi-component systems. Earth and Planetary Science Letters 473, 44-51.

Stout, V.L., Gibon M.D., 1955. Gettering of gas by titanium. Journal of Applied Physics 26, 1488-1492.

Sun, Q., 2009. The Raman OH stretching bands of liquid water. Vibrational Spectroscopy 51, 213-217.

Thomassot, E., Cartigny, P., Harris, J.W., Viljoen, K.S., 2007. Methane-related diamond crystallization in the Earth's mantle: stable isotope evidence from a single diamond-bearing xenolith. Earth and Planetary Science Letters 257, 362-371.

955 Toby, B.H., 2001. EXPGUI, a graphical user interface for GSAS. Journal of Applied
956 Crystallography 34, 210-213.

957 Tschauner, O., Huang, S., Greenberg, E., Prakapenka, V.B., Ma, C., Rossman, G.R., Shen, A.H.,
958 Zhang, D., Newville, M., Lanzirotti, A., Tait, K., 2018. Ice-VII inclusions in diamonds:
959 Evidence for aqueous fluid in Earth's deep mantle. Science 359, 1136-1139.

960 Viljoen K.S., Dobbe, R., Smit, B., Thomassot E., Cartigny P., 2004. Petrology and geochemistry
961 of a diamondiferous lherzolite from the Premier diamond mine, South Africa. Lithos 77,
962 539-552.

963 Weiss, Y. Kiflawi, I., Davies, N., Navon, O. 2014. High-density fluids and the growth of
964 monocrystalline diamonds. Geochimica et Cosmochimica Acta 141, 145-159.

965

966 **Supplementary Materials**

967 **Table 1.** List of bands and species measured by micro-Raman spectroscopy (532 nm-wavelength
968 excitation laser). 1: Reich, 2004, 2: Auer et al., 2008, 3: Anzolini et al., 2018, 4: Men et al., 2014,
969 5: Sun et al., 2009, 6: Brenker et al., 2005, 7: Anthony et al., 2000.

| **Species** | **Raman shift $cm^{-1}$** |
|---|---|
| **Primary inclusions** | |
| Graphite[1] | ~**1580**<br>~2730 |
| O-H stretching vibration[2] | From 3200 to 4000 |
| Breyite[3] | ~**665**,<br>~985,<br>~1056 (weak) |
| CaSiO4-larnite[6] | ~168<br>~540<br>~**848**<br>~**864**<br>~908<br>~984 |
| Ferricopiapite[7] | ~210<br>~460<br>~481<br>~608<br>~**991**<br>~1099<br>~1147 |
| **Secondary inclusions** | |
| Graphite[1] | ~**1580**<br>~2730 |
| Methane [4] | From 2900 to 2930 |
| O-H stretching vibration[5] | From 3200 to 4000 |
| $H_2O$ bending mode[5] | ~**1640** |

SXRD diffraction patterns of selected inclusions in studied diamonds, with the method used in parentheses. **A**) Primary inclusion of *fcc*-(Ni,Fe) alloy, *bcc*-(Fe,Ni) alloy and graphite in sample B20-1 (Lebail method). **B**) Primary inclusion of *bcc*-(Fe,Ni) alloy, *fcc*-(Ni,Fe) alloy, breyite and graphite in sample B20-1 (Rietveld method, except for graphite: Lebail method). **C**) Primary inclusion of NiO in sample B16-1 (Rietveld method). **D**) Secondary inclusion of fcc-(Ni,Fe) alloy, *bcc*-(Fe,Ni) alloy, graphite and *bcc*-(Ni,Fe) alloy in sample B8-1 (Rietveld method. **E**) Secondary inclusion of *bcc*-(Fe,Ni) alloy, *bcc*-(Fe,Ni) alloy and *fcc*-(Ni,Fe) alloy in sample B8-1 (Rietveld method). D and E diffraction patterns display a common, unidentified phase with peaks at 8.085, 9.115, 9.860 and 13.51 2θ. **F**) Secondary inclusion of *fcc*-(Ni,Fe) alloy, *bcc*-(Fe,Ni) and graphite in sample B8-1 (Rietveld method). Synchrotron XRD patterns (wavelength 0.3738 Å) are processed with Rietveld refinement with GSAS (Toby, 2001; Larson and Von Dreel, 2004). Abbreviation: D=diamond. Phase identification of crystalline samples was performed using references from the American Mineralogist Crystal Structure Database (Downs et al., 2003; Cacciamani et al., 2010).

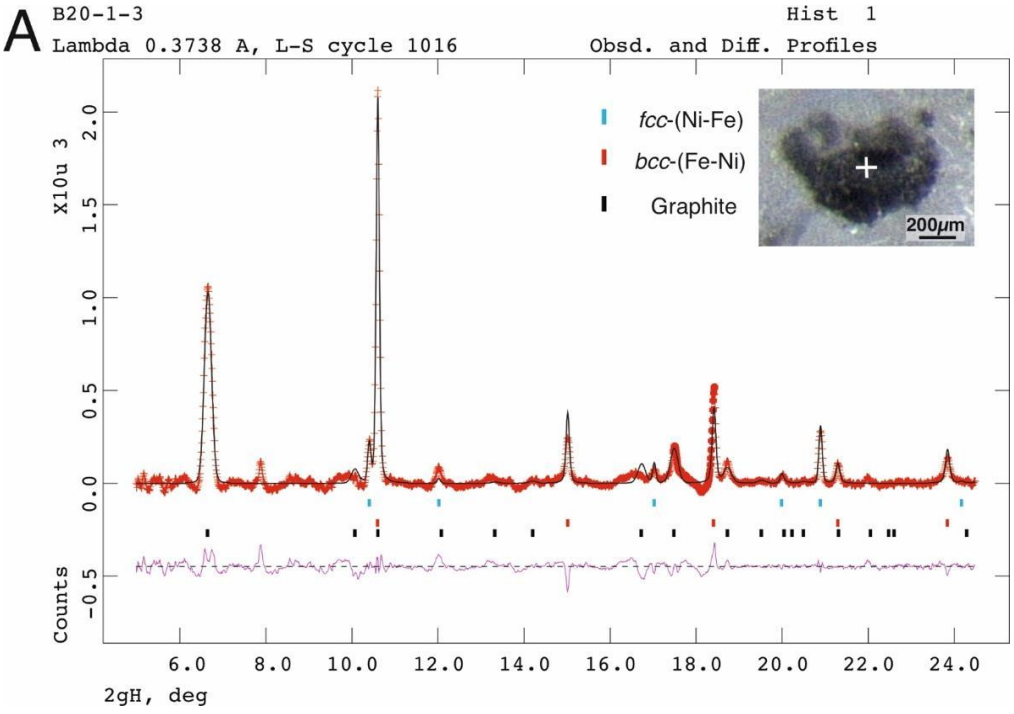

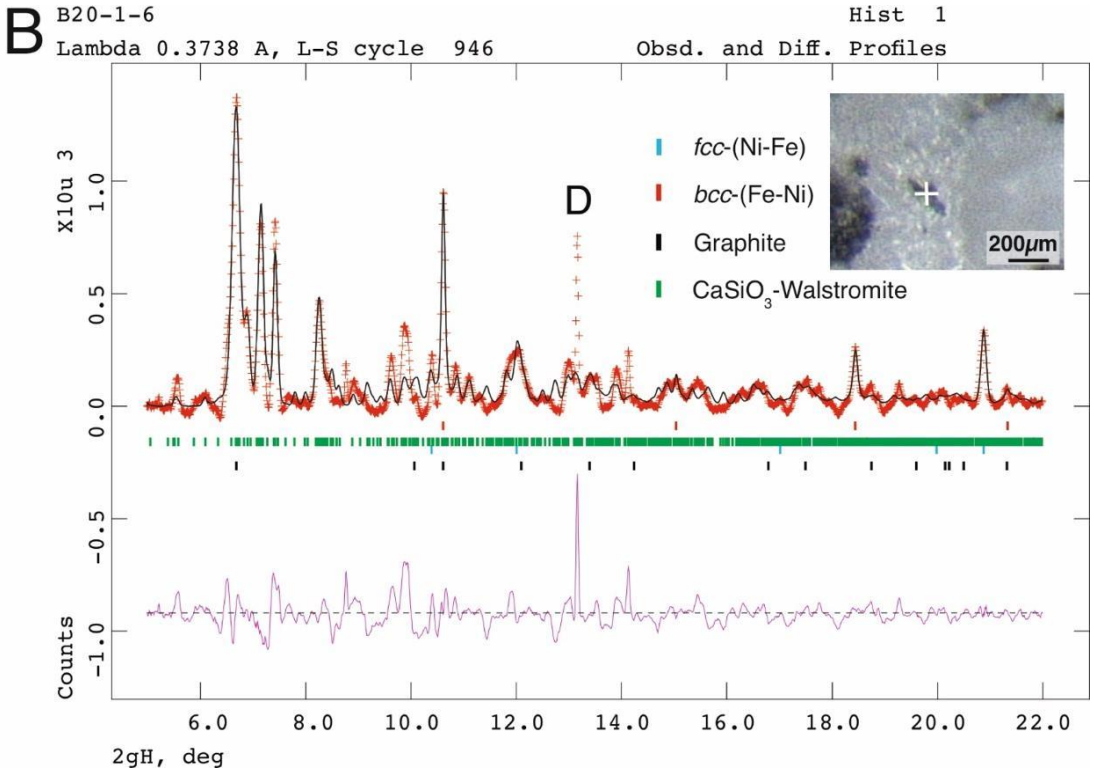
B
B20-1-6
Hist 1
Lambda 0.3738 A, L-S cycle 946
Obsd. and Diff. Profiles
X10u 3
1.0
0.5
0.0
-0.5
-1.0
Counts
D
fcc-(Ni-Fe)
bcc-(Fe-Ni)
Graphite
CaSiO3-Walstromite
200μm
6.0
8.0
10.0
12.0
14.0
16.0
18.0
20.0
22.0
2gH, deg

987

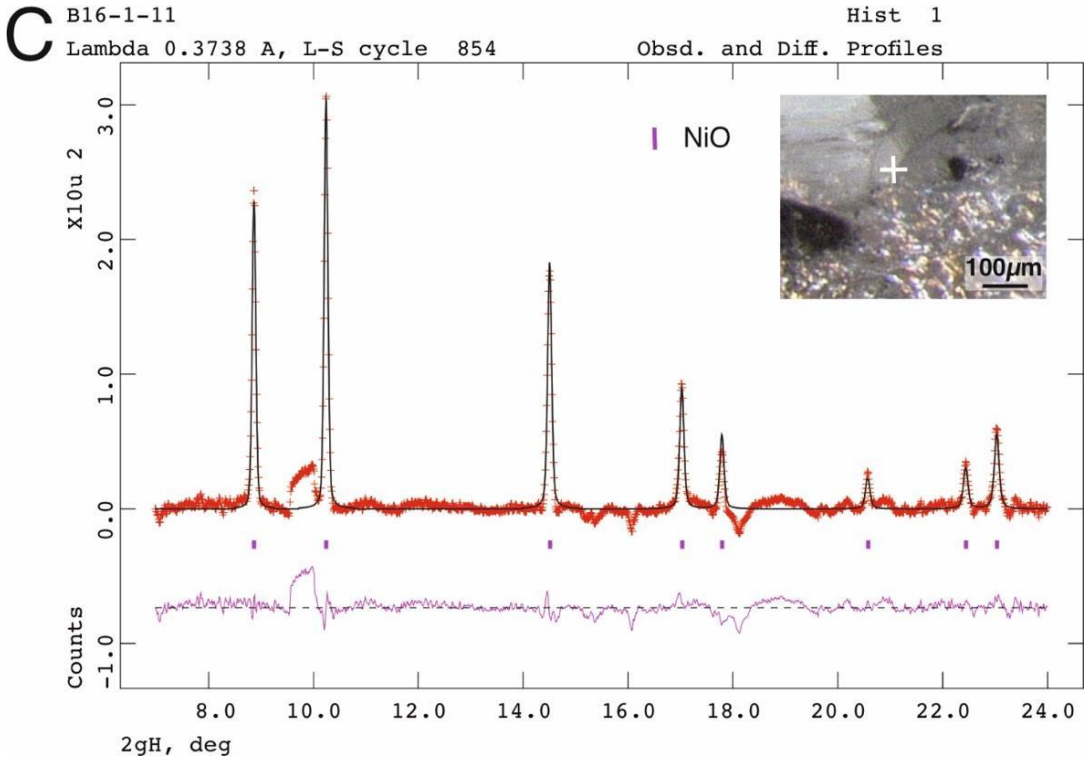
C
B16-1-11
Hist 1
Lambda 0.3738 A, L-S cycle 854
Obsd. and Diff. Profiles
X10u 2
3.0
2.0
1.0
0.0
-1.0
Counts
NiO
100μm
8.0
10.0
12.0
14.0
16.0
18.0
20.0
22.0
24.0
2gH, deg

988

D

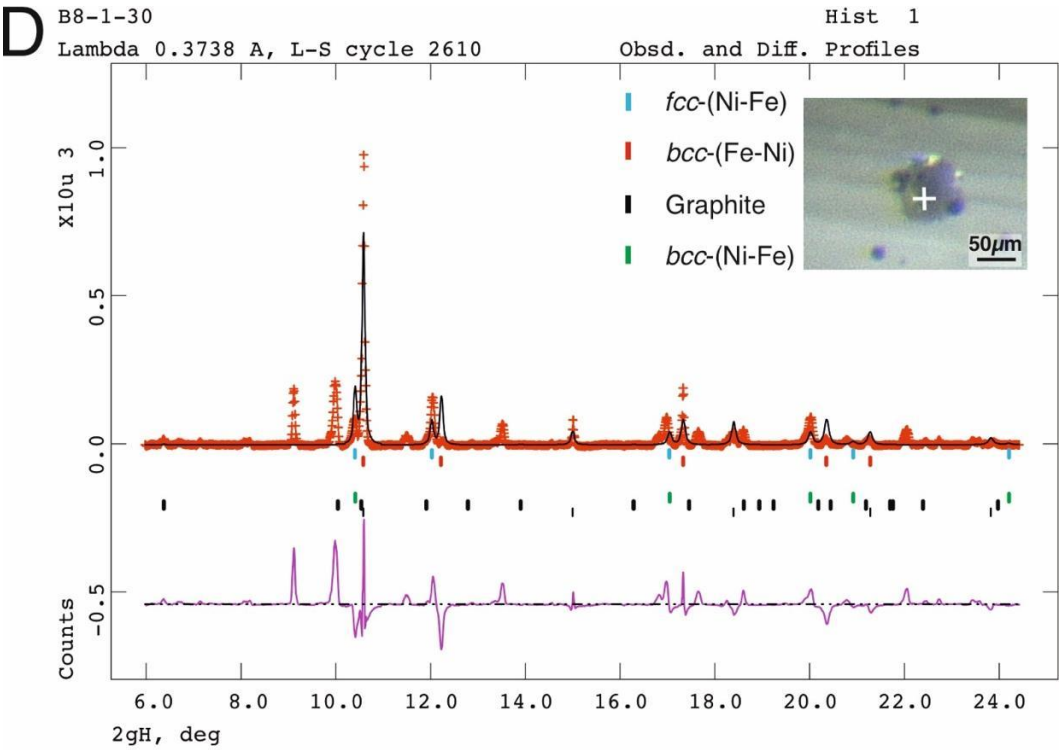
B8-1-30
Hist 1
Lambda 0.3738 A, L-S cycle 2610
Obsd. and Diff. Profiles
fcc-(Ni-Fe)
bcc-(Fe-Ni)
Graphite
bcc-(Ni-Fe)
50μm
X10u 3
1.0
0.5
0.0
-0.5
Counts
6.0
8.0
10.0
12.0
14.0
16.0
18.0
20.0
22.0
24.0
2gH, deg

989

E

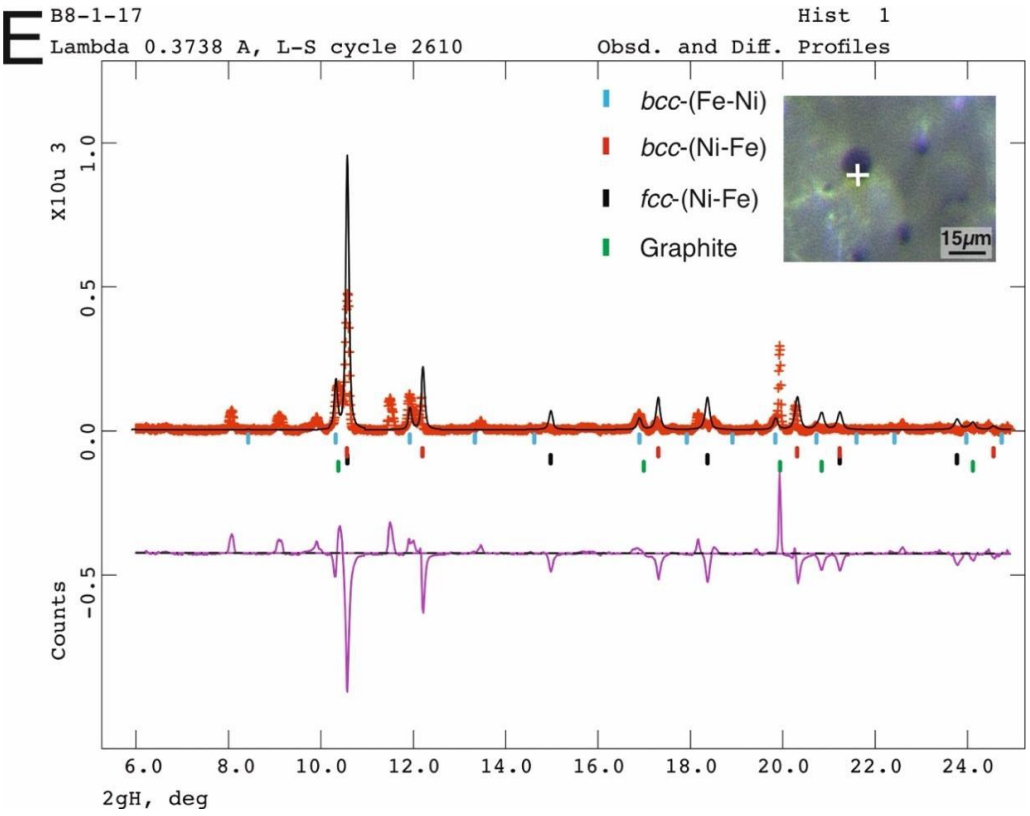
B8-1-17
Hist 1
Lambda 0.3738 A, L-S cycle 2610
Obsd. and Diff. Profiles
bcc-(Fe-Ni)
bcc-(Ni-Fe)
fcc-(Ni-Fe)
Graphite
15μm
X10u 3
1.0
0.5
0.0
-0.5
Counts
6.0
8.0
10.0
12.0
14.0
16.0
18.0
20.0
22.0
24.0
2gH, deg

990

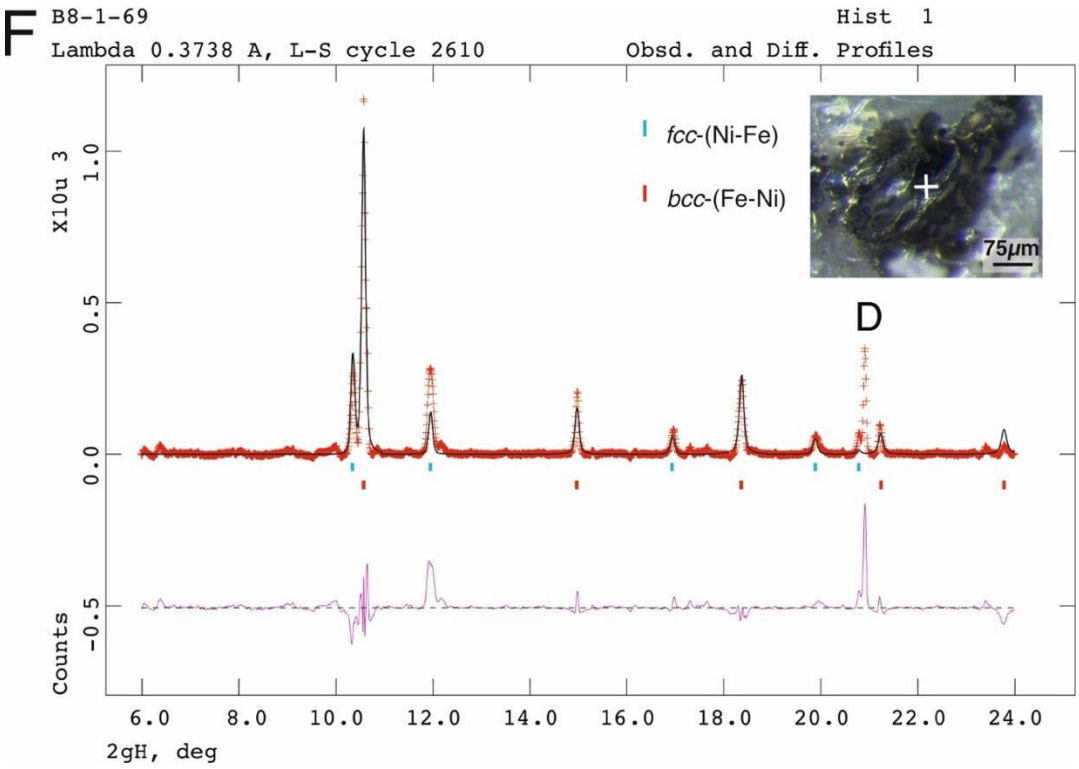
F
B8-1-69
Hist 1
Lambda 0.3738 A, L-S cycle 2610
Obsd. and Diff. Profiles
fcc-(Ni-Fe)
bcc-(Fe-Ni)
75μm
D
X10u 3
1.0
0.5
0.0
-0.5
Counts
6.0
8.0
10.0
12.0
14.0
16.0
18.0
20.0
22.0
24.0
2gH, deg

991